Effect of strain rate on tribological properties of pre-deformed alloys via work function analysis

by

Vikas Kumar

A thesis submitted in partial fulfillment of the requirements for the degree of

Master of Science

in

Materials Engineering

Department of Chemical and Materials Engineering

University of Alberta

Abstract

In industries such as automobile, aerospace and shipping, components made of magnesium and copper alloy could have the chance to bump against other objects during transportation applications. The damage caused by local deformation at high strain rates when other damage processes are involved, e.g. wear or fretting, may result in local micro-cracking and trigger failure of the entire system. The effect of severe deformation on defect formation, e.g., dislocations and microcracks/voids, is influenced by the strain rate. It is therefore, important to study the influences of strain-rate dependent pre-deformation on tribological properties of such alloys.

The first part of the thesis reports a study on effects of tensile strain rate (fast and slow) on hardness, EWF, and tribological properties, including wear and corrosive wear, of pre-deformed AZ31 alloy. It was observed that the strain rate affected the effect of pre-deformation on these properties of the worked AZ31 alloy. A higher strain rate resulted in more deterioration of the alloy's strength and lower resistance due to increased fraction ratio of micro-cracks/voids to dislocations. Corresponding XRD diffraction patterns were obtained in order to determine whether it was possible to obtain relevant information on the fraction ratio of dislocations to micro-voids based on residual strain and understand the observed phenomena. Microstructures of the deformed samples were also examined with electron microscopy. First-principle calculations were conducted to understand relevant mechanisms.

In the second part of the thesis, effects of strain rate and sample thickness on properties of cold-worked brass samples were investigated. We studied influences of the strain rate and sample thickness on strain-softening of deformed brass thin sheets and corresponding wear behavior. Defect-induced strain-softening was observed for cold-worked brass thin sheets, which was affected by the strain rate and sample thickness. A lower strain rate caused smaller decrease in hardness than a higher strain rate for a thicker sheet. However, the situation was reversed for a thin sheet, leading to different variations in the wear behavior.

A residual strain analysis with XRD diffraction was conducted which, however, did not give clear information to explain the above observed phenomena. The samples were then characterized using SEM, which showed that micro-voids or clusters of vacancies existed in the samples along with dislocations. In order to explain the observed phenomena, electron work functions (EWF) of the deformed samples were measured for supplementary information which demonstrated that this parameter can generate meaningful information to help understand the formation of defects and their role in influencing material performance. It has been shown that local change in electron density is caused by the lattice distortion associated with the formation of defects. Both dislocations and micro-cracks/voids decrease EWF. It turned out that EWF is a promising indicative parameter, providing very useful clues to explain the observed opposite trends.

Preface

The study presented in this thesis is a part of a research supervised by Dr. Dongyang Li. The experiments were conducted explicitly in Dr. Dongyang Li's research lab at The University of Alberta.

Chapter-3 of this thesis has been submitted to wear journal (Elsevier) by Vikas Kumar, Lei Li , Gui, Huang, D.Chen, and Dr. Donyang Li entitled " *Looking into changes in work function to understand the effect of strain rate dependent pre-deformation on tribological properties of AZ31 alloy*". Reviewers' comments have been received, the manuscript is currently under revision. I was responsible for performing experimental tests and designing experimental procedure, analyzing data, proposing theoretical models and composing manuscript. The samples were fabricated by research group from Ryerson University (collaborator), Toronto Canada. First-principle calculations were conducted by Dr. Lei Li.

Chapter-4 of this thesis is study of as" *Effects of strain rate and sample thickness on defect-induced work-softening of brass thin sheets and clarification with work function*". I was responsible for performing experimental tests for wear loss, data for results of EWF, SEM and XRD analysis were obtained by Hao Liu, Dr Hailian Gui and me. The data are being organized for a manuscript.

Acknowledgments

I would like to express my sincere gratitude and thanks to Dr. Dongyang Li for his guidance, motivation, enthusiasm, immense knowledge and his outstanding mentorship during my graduate studies at University of Alberta. His mentorship was of utmost importance in providing me a well-versed experience consistently in my research and writing of this thesis. He has been very supportive and has given me the freedom to pursue various projects without objection.

I am thankful to Dr Hao Liu, Dr. Qingyang Li, Dr. Guomin Hua, and Dr. Lei Li for their collaborations in simulations studies and helping me to learn the various characterization tools.

I would like to thank the Department of Chemical and Material Engineering, especially the members of my Research Committee for their input, valuable discussions, accessibility and helpful suggestions. I owe you all, a heartfelt appreciation for guiding me through my tough times.

I would like to thank Natural Sciences and Engineering Research Council of Canada (NSERC), for providing financial support for my research. Finally, and most importantly, I would like to thank my parents and family, for their faith in me and allowing me to pursue my ambition. It was under their watchful eye that I gained so much enthusiasm and ability to tackle challenges head on and endured and survived the experience of graduate school with their unending encouragement and support.

Contents

List of Tables

List of Figures

CHAPTER 1

1. Introduction and background

1.1 Introduction

Theoretical physical strength of materials is not always reached upon testing in the laboratory. Consequently, materials in service may not display the same performance as anticipated. Hence, it becomes the responsibility of engineers to rectify the design of components to curtail the chances of failure. There are several aspects like intrinsic material properties, load or stress system, environment & maintenance, that affect the level of performance of components. The engineers should foresee & strategize for probable failure deterrence of engineering components in advance, which could arise due to design deficits, poor assortment of materials, manufacturing flaws, overloading & exceeding design limits, insufficient upkeep etc. Figure 1 shows a catastrophic failure of an oil tanker, which fractured in a brittle manner by crack propagation at the middle of the tanker.

Figure 1 An oil tanker fractured by crack propagation around its girth [1] .

During a car crash, there's an occurrence of deformation under a wide range of strain rates with locally high strain rate deformation concentrated in crash zones of the vehicle. The deformation strain rates are usually to the order of 10^1 s^{-1} in automobile crash incidents reaching as high as 10^3 s^{-1} [2]. In-addition to the mechanical failure, as mentioned earlier, there are also probabilities for other types of failure. For example, components made of Mg alloys could have the chance to dynamically bump against other objects, and local damage could result in micro-cracking and trigger failure of the entire system.

It is of importance to develop more precise understanding of the crashworthiness of these alloys which is critical to the automotive industry & can be achieved by comprehending the strain rate (10^{-3} –10^3 s^{-1}) material behavior of various lightweight alloys. There are limited

studies on understanding the phenomenon related to the effect of strain rate on wear of pre-deformed materials though work has been done to investigate the stress-strain behavior of these metal alloys from quasi-static to high strain rate conditions [3-4].

Magnesium is considered as the lightest structural metal with attractive properties such as strength-to-weight ratio, machinability, good casting, high thermal conductivity, better dimensional stability, biocompatibility and biodegradability, which make it a good candidate for various industrial applications, particularly for automotive, aerospace, biomedical, and electronics industries [5–11]. Yet Mg alloys still have some drawbacks such as poor strength, low ductility, low wear, and corrosion resistances, etc. which need to be addressed from a materials engineering point of view [11–13]. Lack of sufficient slip systems of Mg negatively affects Mg alloys' fracture toughness and thus limits their applications [14]. This also influences the effectiveness of hardening Mg alloys through the strain-strengthening mechanism. Severe deformation of Mg alloys does not only generate dislocations but may also cause micro-cracks or micro-voids, to accommodate deformation if insufficient dislocations can be produced, especially at high strain rates [15]. Besides, in realistic applications, components made of Mg alloys could have the chance to bump against other objects in transportation applications. The damage caused by local deformation at high strain rates could result in local micro-cracking and trigger failure of the entire system.

In this thesis research, the effect of strain rate on tribological properties of pre-cold worked Mg alloy was investigated via electron work function. More specifically, the scope and objective of the research focuses on:

1. Demonstrating the relationships between EWF and properties, especially tribological and hardness properties, of alloys.
2. Establishing relationships between EWF and strain rate corresponding micro-crack/void fraction to that of dislocations.
3. Investigating influences of strain rate and sample thickness on strain-softening of deformed Mg alloy and brass samples and their corresponding tribological behavior.
4. Evaluating the usefulness of work function as a potential parameter in understanding the defect-involved mechanical state of materials.

In order to understand the influence of strain rate on tribological properties of pre-deformed materials, such as wear, corrosive wear, hardness and corrosion, we examined the pre-deformed Mg samples using SEM. X-ray diffraction analysis was carried out. However, although X-ray diffraction and electron microscopy are often used to characterize defects through diffraction peak broadening and direct observation of dislocations and micro-cracks/voids, these analyses may not provide quantitative information with sufficient clues regarding how the mixture of dislocations and micro-cracks affects tribological properties of deformed Mg alloys.

It has long been recognized that the mechanical property of a material is governed by the electronic behavior of the material and empirical correlations between the electron number. It turned out that EWF is a promising indicative parameter, providing very useful clues to explain the observed opposite trends. EWF is the minimum energy required to move electrons at the Fermi level from inside a metal to its surface without kinetic energy [16-17] .

Furthermore, some surface chemical and physical phenomena [18] have been studied using EWF as a useful parameter because of its sensitivity to surface conditions like adsorption [19–22], surface composition and segregation [23-24], surface morphology, corrosion behavior [25-26] etc. Though EWF appears primarily to depict the behavior of electrons at material surfaces, in actuality it essentially characterizes the interactions along the atoms, mainly the electrostatic interaction between electrons and positively charged nuclei in a metal. Hence, EWF is a fundamental property that can be utilized for forecasting and assessing the bulk properties of materials, which includes the mechanical behavior of metals as well [27-28].

1.2 Thesis organization

Chapter 1 presents a brief introduction to the background of stain rate effect on fracture and tribological properties of alloy in the automotive industry. Also, it provides basic information on EWF as an electronic parameter to define a materials mechanical, wear and corrosion properties.

Chapter 2 is a literature review and background information on strain hardening/cold work, Mg alloys and their slip systems, voids and dislocations in materials, wear and corrosive EWF parameters and how it is related to various material properties like hardness, Young's modulus, wear and corrosion.

Chapter 3 reports a study on influences of strain-rate dependent pre-deformation on hardness, tribological properties and electron work function (EWF) of AZ31 alloy. It was observed that the pre-deformation lowered the alloy's hardness. The pre-deformation at a higher strain rate

caused a larger decrease in hardness and consequently lowered the wear resistance. XRD diffraction analysis and electron microscopy analysis were carried out. However, it did not provide clear clues for explanations, which however could be explained based on corresponding changes in EWF. First-principle calculations were conducted, which were consistent with the experimental observations. This study demonstrates that EWF can provide supplementary information towards clarification of underlying mechanisms.

Chapter 4 discusses defect-induced strain-softening in brass thin sheets, which was affected by the strain rate and sample thickness during cold-work. The investigation in this chapter reports the influence of the strain rates and sample thickness on hardness of deformed brass sheets and their wear behavior. Strain analysis of brass samples was made with XRD and SEM, which showed that micro-voids or clusters of vacancies existed in the samples along with dislocations. However, it was very challenging to quantify the ratio of micro-voids to dislocations, making it difficult to clarify relevant mechanisms. In order to explain the observed phenomena, electron work functions (EWF) of the deformed samples were measured, which was turned out to be a promising indicative parameter, providing useful clues to explain the phenomena observed during the experiment.

Finally, Chapter 5 outlines the key conclusions of the research and its corresponding future work.

CHAPTER 2

2. Literature review

This chapter gives a written audit with respect to essential properties of magnesium and its slip framework, impact of strain rate on material behavior, EWF parameters, and how they impact different material properties like hardness, Young's modulus, wear and corrosion.

2.1 Fundamental aspects of magnesium alloy

Among all elements, magnesium (Mg) is the 4th most available element in the Earth, following iron, oxygen and silicon [29]. Table 1 depicts the various properties of magnesium. Due to low specific gravity of 1.74, magnesium is considered to be the lightest structural metal which offers the automobile industry an increase in fuel economy of up to 7% corresponding to10% reduction in vehicle weight [30]. Table 2. shows the typical mechanical properties of automotive sheet materials and equivalent Mg yield and fatigue strength. The properties of magnesium can be enhanced by alloying with other metals such as aluminum, zinc, and silicon.

Table 1 Chemical and material properties of magnesium.

Chemical and Material Properties	Values
Density	**1.738 g.cm -3 at 20ºC**
Melting point	**650ºC**
Boiling point	**1103ºC**
Crystal structure	**close-packed hexagonal**
Specific heat	**1025 J.K $^{-1}$.kg at 20ºC**

Table 2 Typical mechanical properties of automotive sheet materials and equivalent Mg yield and fatigue strength [30]

	Density (g/cm3)	Elastic modulus (GPa, typ.)	Yield strength (MPa, typ.)	Mg equivalent yield strength (MPa)
Steel (mild)	**7.7**	**210**	**250**	**78**
Steel (DP980)	**7.7**	**210**	**910**	**285**
Al sheet (5182-O)	**2.7**	**69**	**120**	**87**
Al sheet (6022-T43)	**2.7**	**69**	**135**	**98**

2.2 Slip systems

Mg has low ductility and thus reduced formability in polycrystalline products, because Mg crystal has a hexagonal close-packed crystal structure, which is inherently anisotropic and has a limited number of independent slip systems.

Similarly, in case of magnesium alloys, there are only limited slip systems available to accommodate plastic deformation due to their HCP structure with a c/a ratio of approximately 1.62 [31].

Slip is the glide of dislocations along definite crystallographic (slip) planes in specific crystallographic (slip) directions, resulting in atomic displacement. Permanent deformation is caused by accommodation of the imposed strains caused by collective glide of dislocations on diverse slip systems (i.e., slip plane and direction) [32]. As observed by Taylor, more than five independent slip systems are required to achieve uniform distortion in a haphazardly oriented polycrystalline metal [33]. There is a transformation in the orientation of the slip system from one crystal to another which thwarts the glide of a dislocation from one grain to another upon reaching the grain boundary. Hence, it becomes vital that slip systems exist in order to allow continual slip activity thereby averting failure of the material. [33-34]. Because of very different CRSS values of the slip systems [35], HCP crystals are unable to provide adequate independent slip systems to fulfill the Taylor criterion [34-35] as compared to the body centered cubic (BCC) and face centered cubic (FCC) crystal structures.

There is a remarkable improvement in ductility of magnesium alloys at elevated temperatures which can be explained by the following phenomenon. When magnesium alloys are kept at room temperature, they only have three independent slip systems & twinning is responsible for accommodating the remaining deformation [36–38]. Figure 2 depicts the different slip systems in HCP materials. However, at elevated temperatures, adequate independent systems get generated as additional slip systems become active thereby fulfilling the von Mises-Taylor criterion [36–38].

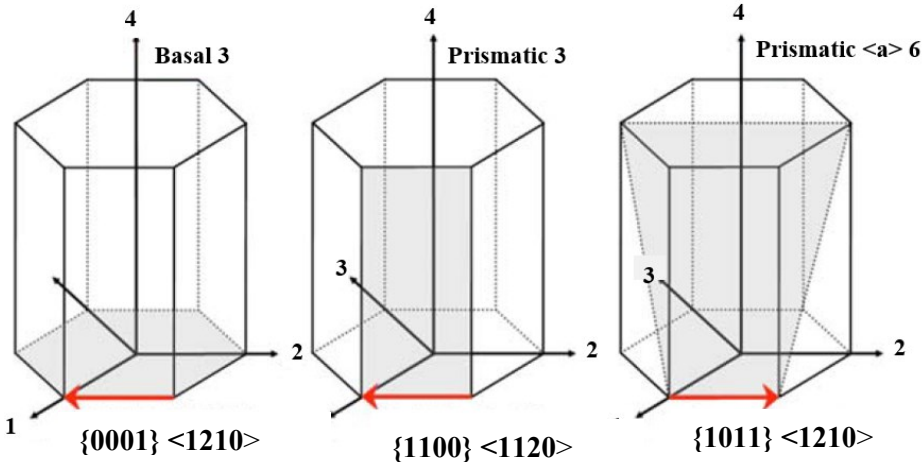

Figure 2 Slip system families in hexagonal structures [39].

2.3 Twinning

Another important deformation mode for Mg alloys, especially at room temperature [40–41] is twinning. It has been described by Bilby et al. [42] that twin is a region which experience

a homogenous shape deformation in such a way that both parent structure and deformed one are identical but have different orientations as can be seen in Figure 3.

There is often a comparison between twinning & slip in terms of their similar kinetic characteristics involving simple shear. However, there are some vital differences that differentiate slip from twinning. Twinning is directional which means that it can only be activated by shear in a particular direction whereas slip can be activated in both the positive and negative senses of an applied shear stress.

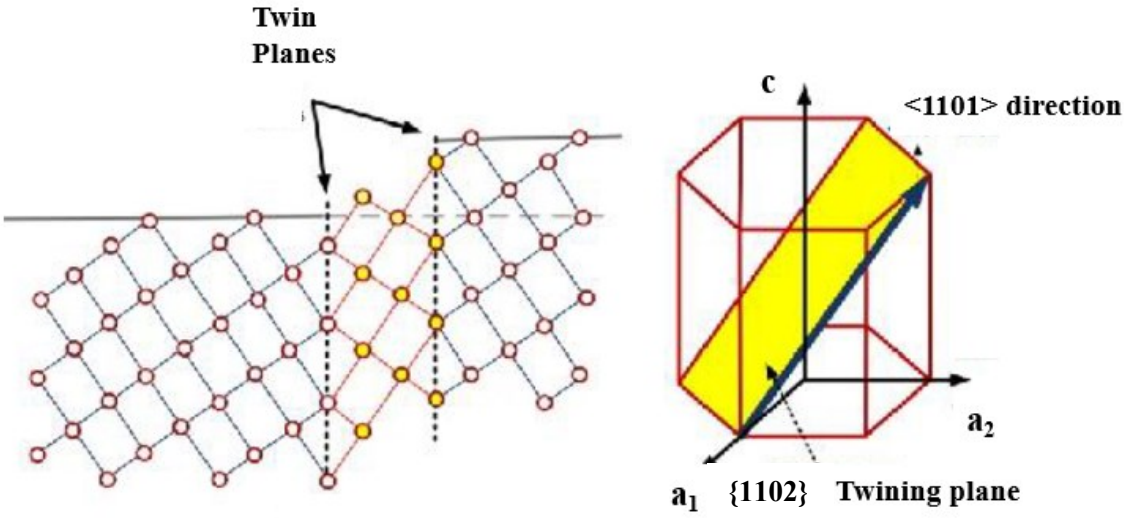

(a) (b)

Figure 3 Schematic representation of (a) forming twin, (b) extension twining in Mg crystal [43]

Due to lack of independent slip systems at lower temperatures, twinning is more noteworthy at low temperatures although it can happen at all temperatures. Twinning systems are significantly influenced by the c/a ratio amongst the different HCP materials [37, 43–44] . The two most common twinning systems in Mg alloys are the extension twins activating on the $\{1\bar{1}20\}$ planes in the $\langle\bar{1}011\rangle$ direction and contraction twins, which occur on the $\{10\bar{1}1\}$ plane in the $\langle\bar{1}012\rangle$ direction [35, 37, 45].

2.4 Effects of strain rate on the material behavior of cold-worked alloys

There has been a substantial increase in research focusing on the strain rate sensitivity of materials like metals [47], ceramics [48], polymers [49], concrete [50], or muscle tissue [51] as constitutive behavior is exhibited by most of the materials experiencing deformation at different strain rates. For instance, studies have been conducted to analyze the effects of varying strain rate on the dominant deformation mechanism of magnesium alloys. Dislocation creep has been found to be the primary catalyst for deformation at lower strain rates ($0.1s^{-1}$) whereas dislocation glide & twinning are the leading mechanisms at higher strain rates, as demonstrated by Ishikawa et al. [52–53] during the compression tests performed on AZ31 and AZ91 materials.

The effect of severe deformation on defect formation, e.g., dislocations and micro-cracks/voids, is influenced by the strain rate. According to dislocation dynamics [54–55], at high strain rates, the equivalent mass of dislocations increases considerably, increasing the difficulty of generating dislocations during deformation and the motion of a dislocation can

be regarded as the motion of an equivalent mass. The equivalent mass of a moving dislocation is velocity dependent, which increases with increasing the velocity, as the following equation expresses:

$$m^* = m_0\left(\frac{1}{\sqrt{1-(v/v_0)^2}}\right)$$

where v is the velocity of the dislocation, v_0 is the velocity of sound, and m_0 is the equivalent mass of a screw dislocation at rest. At high strain rates, the equivalent mass of a dislocation increases, making it is hard to be driven. In this case, micro-cracks/voids are generated in order to accommodate the deformation. As a result of the decrease in dislocation density ($\rho_{dislocation}$) and formation of more micro-cracks/voids, the fraction ratio of dislocations to micro-cracks/voids decreases with the strain rate i.e.

$$\dot{\varepsilon}\uparrow \Rightarrow \frac{\rho_{dislocation}}{\#Micro-cracks/voids}\downarrow$$

Moreover, micro-cracks or micro-voids may occur to accommodate the deformation. The locally formed defects could affect, e.g., local wear and corrosion events, possibly initiating local damage that may trigger global failure. Thus, it is of interest to investigate effects of pre-deformation at different strain rates on the resistance of Mg alloys to failure, e.g., wear and corrosion. The effect of strain rate on properties of deformed Mg alloys should be related to the ratio of dislocations to micro-cracks/voids caused by the dynamic deformation.

Also, cold-work generally strengthens metallic materials due to dislocation interference, resulting in barriers to dislocation movement. The strain-hardening is influenced by the strain rate. Strain-hardening effect is also influenced by sample dimensions. For thin metal sheets, due to reduced lattice confinement, dislocations could move to the sample surface and annihilate there to minimize the strain energy. Cold-work may involve dislocation generation, micro-void formation and micro-cracking, influenced by both the strain rate and sample dimensions. Thus, the effect of cold work on hardness of materials could be beyond our expectation, e.g., strain-softening may occur. For thin metal sheets or foils, it has been reported that heavy deformation involves formation of both dislocations and micro-voids. For multi-phase alloys, void formation could be promoted during plastic deformation [56 –57]. Thus, the strain-hardening effect may be altered or reversed, which could be more obvious for thin sheets due to less crystal lattice constraint to dislocations and strain-induced softening may occur at low strain rates. For thin metal sheets or foils, it has been reported that heavy deformation involves formation of both dislocations and micro-voids. Kojima and Fujii [58] demonstrate that the formation of voids in thin gold foils play an important role during plastic deformation.

2.5 Wear and corrosive wear

When a relative mechanical motion at the surface of solids causes the removal of material, such damage is termed as wear. The dynamic contact with solid, liquid or gas on the solids may result in this type mechanical attacks. Usually there are high costs associated for repair

of components and replacement parts due to progressive loss of material from the primary surface caused by wear, which makes it highly undesirable.

Erosive wear, abrasive wear, adhesive wear, fretting and corrosive wear are the foremost modes of wear. It is estimated that abrasive wear is responsible for half of all wear failures, followed by adhesive wear for 15% of wear failures, and the remaining by other forms of wear[59]. According to the Archard (1953) equation, the wear rate of an engineering material can be estimated using the equation below:

$$V = K\frac{L * S}{H}$$

where:

V: The wear volume loss

H: Hardness of the material

L: Normal Load

S: Sliding distance, and

K: Wear coefficient

The damage that is caused by synergistic attack of corrosion and wear or wear in a corrosive environment is defined as corrosive wear or tribo-corrosion. This type of attack may result in a notably high wear rate [60 –61] as the wear and corrosion mutually affect each other, which is often encountered in various industrial processes. The difference between material loss caused by corrosive wear and that caused by each of wear and corrosion damage individually

is the material loss due to the synergy [60]. The total damage by corrosive wear may be expressed as:

$$V_{ct} = (V_{lw} + V_{lc} + V_{ls})$$

where:

$V_{ct:}$ Total loss in volume due to corrosive wear

$V_{lw:}$ Loss in volume due to wear

$V_{lc:}$ Loss in volume due to corrosion

$V_{ls:}$ Loss in volume resulted by synergy of wear and corrosion

The wear-corrosion synergy consists of two parts:

i. The increase in wear rate due to corrosion (r_{c-w})

ii. The increase in corrosion rate due to wear (r_{w-c})

$$r_{synergy} = r_{c-w} + r_{w-c}$$

Understanding that material's both wear resistance and corrosion resistance are intrinsically dependent on its EWF, it is promising for us to use this fundamental parameter to characterize the corrosion-wear synergy.

Usually, the contact between the metal or alloy and the corrosive environment is restricted by a surface oxide film existing on many metals and metallic alloys which reduces corrosion. As explained above, the situation in magnesium and its alloys is the same where the surface oxide fortifies the alloy. When there is the presence of wear, corrosion is accelerated due to removal

of surface oxide film from the surface. Also, the material becomes more anodic due to the plastic deformation introduced by wear [60].

The strained and unstrained zones having different electrochemical potentials may also contribute to the increase in material loss in corrosive wear as these microelectrodes can intensify corrosion by promoting micro-galvanic corrosion. The concentration of metallic ions in the vicinity of the worn surface is also reduced and the corrosive environment is increased by the wear, causing a greater rate corrosion reaction rate as the transfer of ions to the cathode is accelerated [60].

Wear itself can be promoted by corrosion. There may be a generation of products like porous oxides on the surface, which are weaker than the original alloy. As a result of the easy removal of the poor surface oxide scale, the resistance of the material to frictional force and thus wear could be considerably reduced. Additionally, hydrogen embrittlement phenomenon in the surface layer of the metal may become prevalent, resulting in lowered toughness and resistance to wear in the corrosive environments [60].

The general wear testing systems that are used in dry condition can be utilized to evaluate the performance of a material under corrosive wear condition, i.e. performing the wear test in a corrosive solution of interest.

2.6 EWF

Although X-ray diffraction and electron microscopy are often used to characterize defects through diffraction peak broadening and direct observation of dislocations and micro-cracks/voids, these analyses may not provide quantitative information with sufficient clues regarding how the mixture of dislocations and micro-cracks affects tribological properties of deformed Mg alloys. Recent studies [16, 17, 62–65] show that elastic and plastic deformation and defects in materials can be reflected by the electron work function (EWF) [17], which is the minimum energy required to move electrons inside a metal to its surface without kinetic energy as shown in figure.4. Such reflection is ascribed to local change in electron density caused by the lattice distortion associated with the formation of defects. Not only to defects but, due to the extensive application of the Kelvin probe (KP) technique [18], there has been increasing interest in both experimental and theoretical investigation of the relationship between electron work function (EWF) and mechanical deformation during the last three decades. EWF is also correlated to the mechanical behavior of materials [16, 59, 61–63]. Thus, it is possible to look into the effect of strain-induced defects on tribological properties (wear, corrosion, and corrosive wear) of the Mg and Cu alloys that are pre-deformed at different strain rates from the view-point of electron behavior via EWF analysis. EWF is determined by the valence electron density [64–65], which governs the metallic bond strength and dislocations activities.

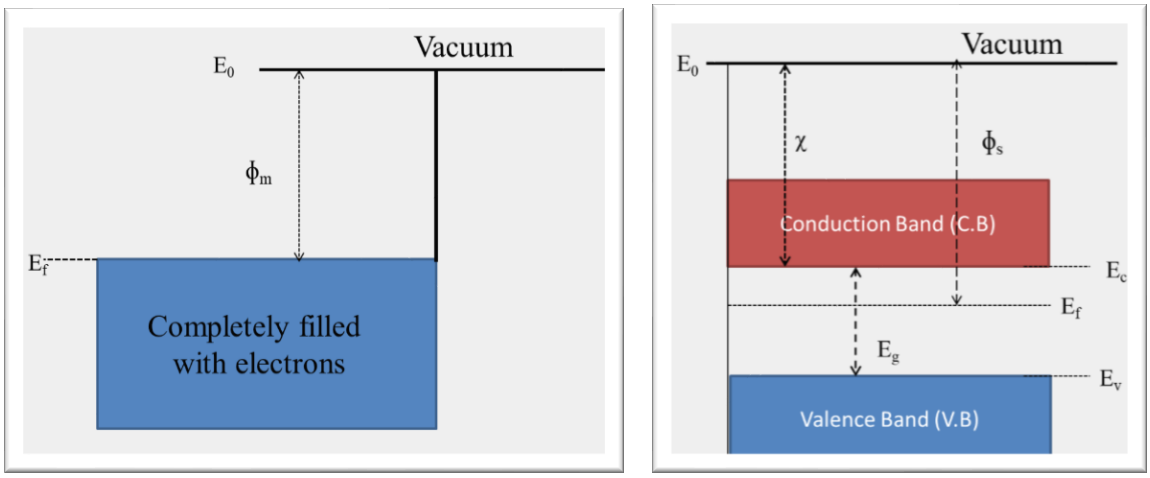

(a) (b)

Figure 4 Band diagram of metal (ϕ_m is the work function of metal). Xb. Band diagram of semiconductor (ϕ_s is the work function of semiconductor).

2.7 Correlation between properties of materials and EWF

Micro-voids also lower EWF due to decreased electron density when the solid becomes porous; but the decrease in EWF caused by voids may not be as large as that caused by dislocations, which introduces large local lattice distortion. Allowing for the fact that EWF is closely correlated to mechanical properties [59, 61–62, 66–67], it helps understand strain-induced variations in hardness and relevant mechanisms, i.e., whether the deformation is achieved primarily by dislocation processes, void formation, or both in thin sheets. The correlation between EWF and various atomic properties like electronegativity and ionization energies is well known [72]. It is anticipated that there is a correlation between EWF and the physical and chemical properties of materials since EWF is a fundamental electronic property

of metallic materials.

2.8 Relationship between EWF, Young's modulus and yield strength

It has been shown that there is sixth power dependence of Young's modulus on EWF [16] as depicted in Figure 5 below. Plastic deformation is caused when the threshold of the critical stress above which dislocations are generated is reached which is also known as yield strength. This yield strength is inherently reliant on atomic bonding although it is affected by many other aspects like activated slip systems. It has been shown in the Figure 6 the yield strength of metals also exhibits a similar relation with EWF as Young's Modulus [63].

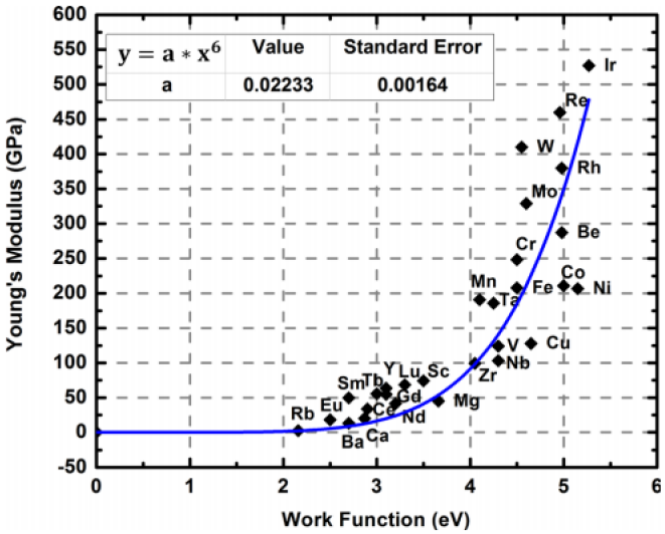

Figure 5 Collected experimental data and theoretical curve of Young's modulus and EWF relationship of polycrystalline metals [16].

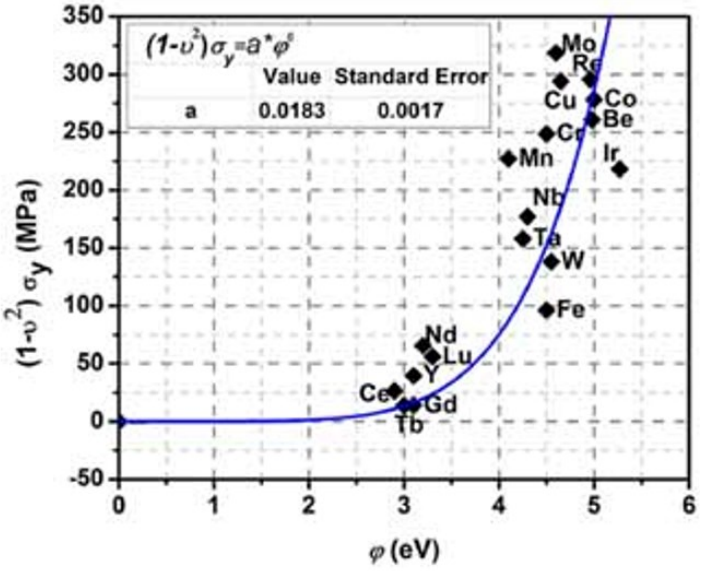

Figure 6 Relationship between EWF and yield strength [63].

2.9 EWF and Hardness

The resistance to plastic deformation of a solid is termed as hardness. Hardness is nearly proportional to the yield strength despite being an integrated property of numerous mechanical properties like toughness, strength, plasticity & elastic stiffness. Hence, EWF can be correlated to hardness as well [63].

The dependence of hardness on EWF is the same as that of the yield strength because of the linear relationship existing between the yield strength & hardness. It is important to take into consideration that there are many other external factors like possible texture, heat treatment, cold working etc. that also play an important part in affecting the yield strength and hardness.

There is an explanation for the physical mechanism causing these correlations between EWF

and intrinsic yield strength and hardness. The yield strength and hardness, which are caused by the activation energies for dislocation motion, are meticulously related to the electronic state. During a higher EWF, a larger catalyst force is required for dislocation movement and electron rearrangement as a higher value of EWF leads to more stability of electron states in metallic bonds. Hence it becomes imperative that when EWF is higher, the resistance of a metal to mechanical deformation should be consequently larger.

2.10 EWF and Wear

The past before the occurrence of quantifiable wear can be inspected by EWF measurement as it has been observed to be the most sensitive technique to changes in surface condition. The sensitivities of the three methods to wear schematically are shown in Figure 7. The conventional techniques of detecting the onset of wear like weight loss measurement and morphological observation, specifically under low load pose huge challenges. Thus, EWF is a promising parameter for determining wear initiation, especially for light-load contact and nano/micro-systems.

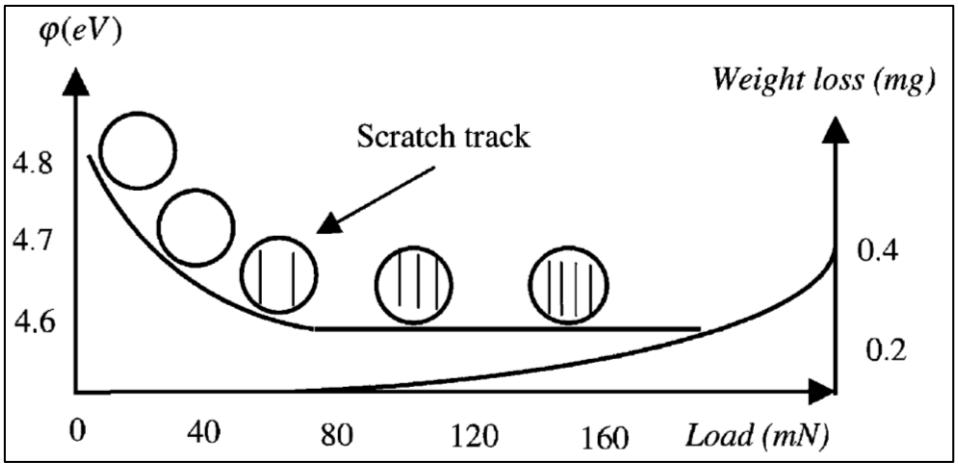

Figure 7 A schematic illustration of the sensitivities of three methods to wear: weight loss measurement, morphological observation, and EWF measurement [73].

The wear resistance can also be reflected by EWF via the relation between wear and hardness. Attempts have been made to establish a correlation between hardness and electron work function, which has the following form [63].

$$H \propto \varphi^6(1-v^2)$$

Substituting the above equation hardness in Archard's equation:

$$WL = K_w \frac{F.l}{H} \propto \frac{F.l(1-v^{2)}}{\varphi^6} = K_{w\varphi} \frac{F.l(1-v^{2)}}{\varphi^6}$$

This equation suggests a reverse sextic relation between the sliding wear loss and work function of the target material. We may use a coefficient, $K_{W\varphi}$, to replace K_W when the hardness is represented by the work function.

2.11 EWF and Corrosion

The corrosive behavior of materials is intricately linked to EWF, which is a measure of electrochemical stability of a material. Materials with higher EWFs usually possess higher resistances to corrosion. As demonstrated in Figure 8, the sample surface of 304 stainless steel with highest EWF was found to have the most positive corrosion potential.

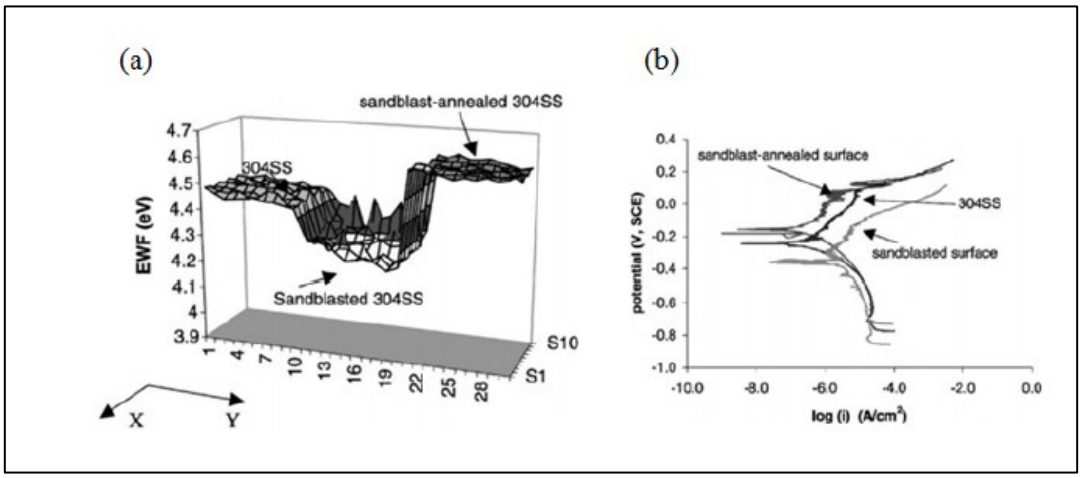

Figure 8 (a) Surface EWF of different specimen (b) Polarization curves of different specimens in a 3.5% NaCl solution [74]

However, corrosion is also influenced by surface films and solid/solution or surface interfaces, which may alter the work function thus the corrosion behavior.

For many other materials like aluminum alloys [75], copper alloys [76], Ti/Mg-Al dissimilar materials [77], etc. extensive work has also been conducted. Invaluable information to comprehend the corrosion behavior of the materials has been provided by the KPFM technique and EWF measurements [78–79].

CHAPTER 3

3. Effect of strain rate on the tribological properties of AZ31alloy

In this study, effects of tensile strain rates ($10^{-1}s^{-1}$ and $10^{-4}s^{-1}$) on hardness, EWF, and tribological properties of AZ31 alloy were investigated. Corresponding XRD diffraction patterns were obtained in order to determine if it is possible to obtain relevant information on the ratio of dislocations to micro-voids based on residual strain analysis and understand the observed phenomena. Microstructures of the deformed samples were also examined with electron microscopy. As shown in the article, the above analyses did not provide sufficient and clear clues to explain the observed phenomena which can, however, be achieved to a certain degree based on corresponding changes in electron work function, demonstrating that this parameter can generate meaningful information to help understand the formation of defects and their role in influencing material performance.

3.1 Experimental method

Samples of AZ31 alloy used for the study experienced standard tensile tests up to fracture at two strain rates, 10^{-4} s^{-1} and $10^{-1}s^{-1}$. Representative stress – strain curves are illustrated in Figure 9.

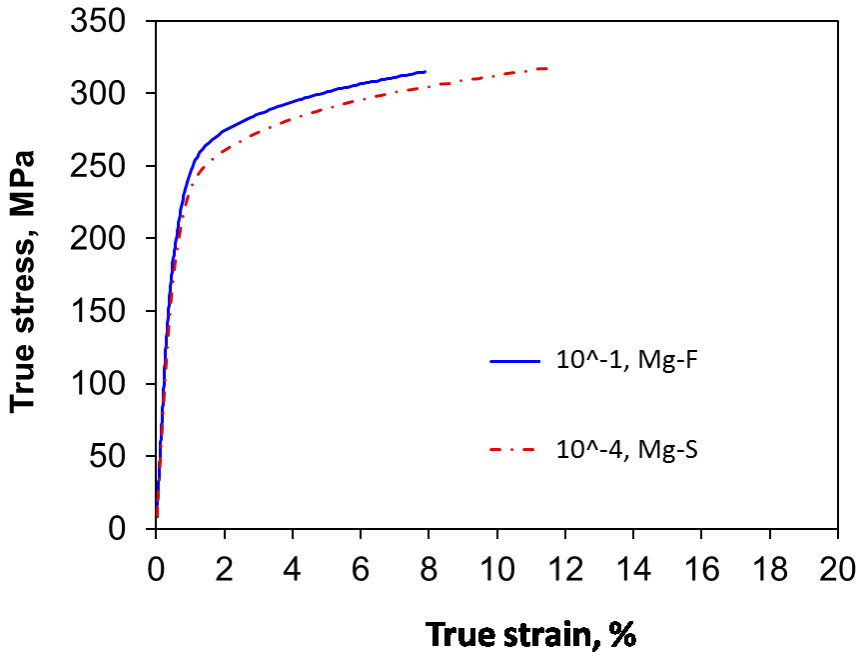

Figure 9 Representative stress – strain curves of samples deformed at strain rates, 10^{-4} s^{-1} and $10^{-1}s^{-1}$, respectively. Average elongations of samples deformed at the two strain rates are 17% and 7%, respectively.

Samples deformed at the two different strain rates are denoted as

Mg-S: the sample deformed at the low strain rate of 10^{-4} s^{-1}

Mg-F: the sample deformed at the high strain rate of $10^{-1}s^{-1}$

After the tensile tests, surfaces of the samples were lightly polished using SiO_2 sand papers of different grades, rinsed and quickly dried using an air blower. Hardness of the sample was measured using an Indentec Hardness Tester (Zwick Roell ZHR, UK). Each reported hardness value is an average of at least three measurements with standard deviation around 9~13%. Zones near the fractured surface and those about 10 mm away from the fractured surface were

observed under a scanning electron microscope (after etching using dilute ammonium hydroxide). X-ray diffraction patterns of the zones near the fractured area were obtained using a XRD system (D8 DISCOVER, Bruker). EWFs in different locations were measured using a scanning Kelvin probe (KT Technology, UK). Each reported EWF value is an average of at least five measurements. Wear tests were performed on a pin-on-disc wear tester (CSEM Instruments, Neuchatel, Switzerland) at room temperature (20°C). The disc was the sample and the pin was a silicon nitride ball with 6 mm in diameter. All tests were performed at a sliding speed of 0.5 cm/s along a circle path of 1.0 mm in diameter under a normal load of 2 N over a sliding distance of 18 m. Wear tracks and corresponding volume losses of the samples were determined using a confocal microscope (ZeGage 3D optical profilometer, Zygo Corp.). At least three tests were performed for each reported average value of wear loss. Corrosion behavior (material loss) of the Mg alloy was measured by immersing samples in tap water for different periods of 60, 120, 180 min, respectively. At least three tests were performed for each reported average value of corrosion loss.

3.2 Computational modeling

First-principles calculations were conducted to investigate effects of dislocations and vacancies on electron work function using the Vienna Ab initio Simulation Package (VASP) with projector-augmented wave (PAW) potential [76–80]. The generalized gradient approximation (GGA) with the exchange-correlation function of Perdew-Burke-Ernzerhof (PBE) was employed[85]. A cutoff energy of 400 eV and dense k-points sampling with a Methfessel-Paxton smearing of 0.2 eV was used to guarantee high numerical accuracy for

both energy and stress optimization. For sufficient convergence, the tolerance value in the geometry optimization is 1.0×10^{-5} eV/atom, which is small enough to ensure accuracy of the calculations. Due to the existence of the defects, e.g., vacancies or dislocation, the spin-polarized set is necessary for our calculations. The global break condition for the electronic self-consistency was chosen as 1.0×10^{-5} eV per supercell for all calculations. To investigate the surface, we constructed 6×1×5 supercells of Mg (a = 19.2564 Å, b = 3.2094 Å, c =26.0525 Å) on its primitive cell (a = b = 3.2094 Å, c = 5.2105 Å). This Mg supercell was cleaved along the (001) facet so as to build the Mg-surface with the vacuum layer of 15 Å for the calculation of work function. Thus, total thickness of the surface model is equal to about 41.05 Å. Such a size should be large enough for calculating the system's properties under study.

3.3 Results and discussion

3.3.1 Effect of strain rate on hardness

Figure 10 depicts locations of the Mg alloy sample that experienced a tensile test, where various properties were measured. Location 5 denotes the area near the fracture surface. The sample surface was marked with square grids, which were used to determine the local strain using the following equation

$$Strain\ (\%) = \frac{l - l_0}{l_0} * 100$$

where l_0 is the original length of the grid before deformation and l is the length after deformation.

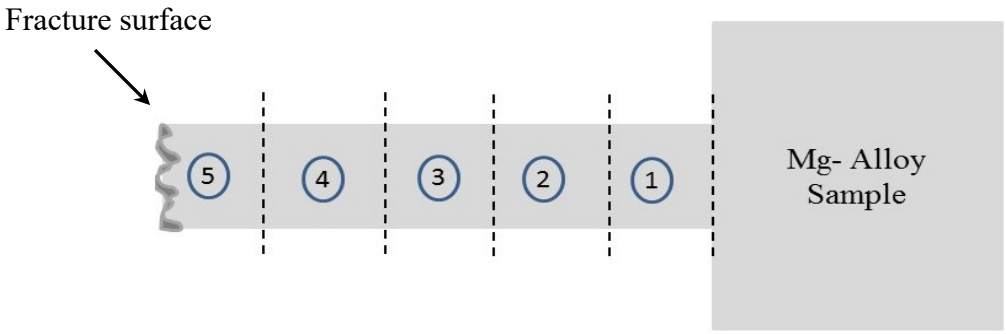

Figure 10 Positions of the Mg alloy where various properties were measured.

It is depicted in Figure 11 that the strain is larger in the location near the fracture surface and gradually decreases in locations away from the fracture surface. The larger strain in the location closer to the fracture surface should result from increased density of defects, e.g., micro-voids and dislocations. Micro-voids increased local stress concentrations, leading to eventual failure as a result of micro-void growth and coalescence.

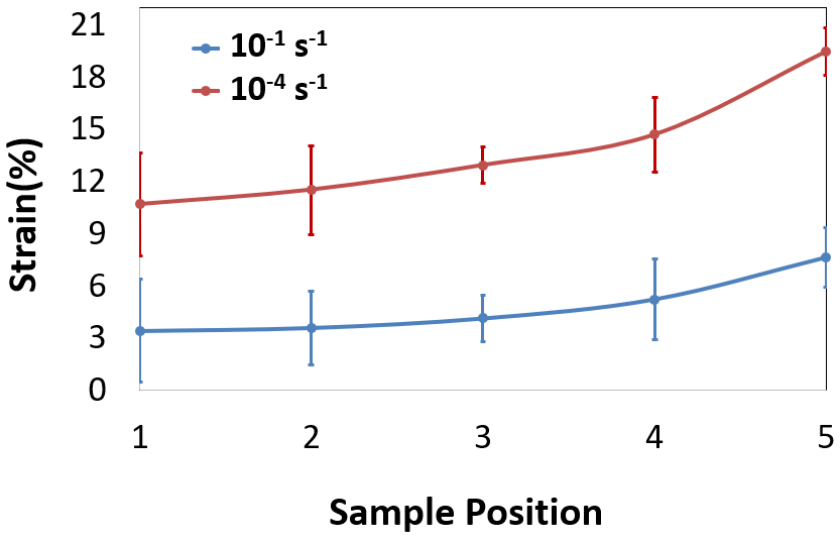

Figure 11 Strains at different locations of AZ31 samples after tensile tests at two different strain rates.

Figure 12 illustrates decreases in hardness with respect to an increase in strain. The decrease becomes larger in locations near the fracture zone where the strain is larger. The decrease in hardness should result from the formation of micro-voids, which generate stress concentrations, reducing the stress-bearing capability and thus the resistance to deformation. The sample pre-deformed at the higher strain rate showed a faster decrease in its hardness, especially near the fracture surface, than the sample pre-deformed at the low strain rate.

It is suggested that at low strain rates the plastic flow is influenced by thermal activation[15,54]. When dislocations move in a crystal lattice, thermal vibrations may assist the dislocations to overcome short-range barriers resulting from dislocation interactions. However, at higher strain rates the barriers hinder the plastic flow. This happens because there is not sufficient time for the thermodynamic fluctuation to play an effective role in assisting the movement of dislocations. Thus, at higher strain rates, the resistance to the motion of dislocations increases, resulting in elevated yield strength and reduced fracture strain. Consequently, the plastic deformation is restricted, while more micro-cracks and voids are introduced to accommodate the deformation (see Figure 13). As the strain rate is increased, the ratio of the fraction of micro-cracks/voids to that of dislocations increases, leading to a decrease in hardness because micro-cracks/voids generate stress concentrations and reduce the stress-bearing capability.

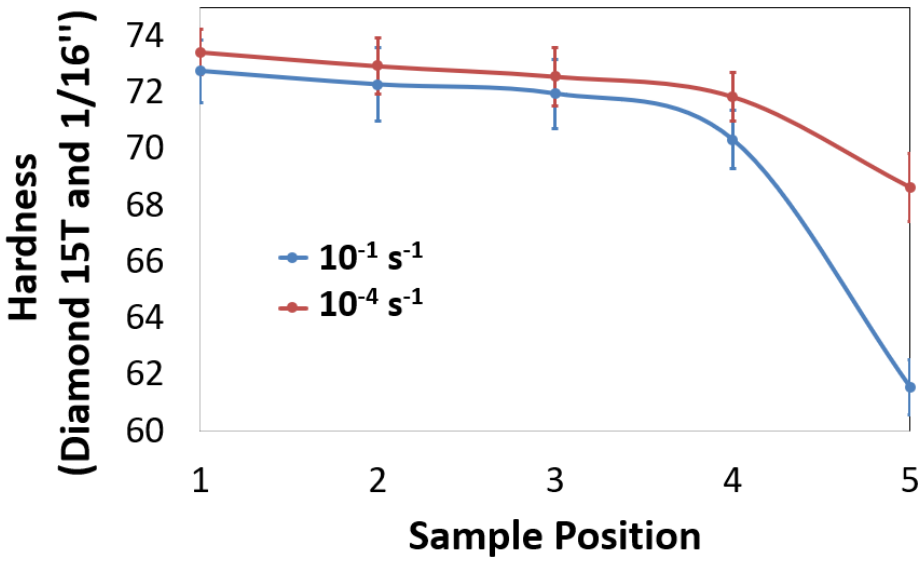

Figure 12 Hardness values measured in different locations of Mg alloy samples, corresponding to different strains (given in Fig.2), deformed at two different strain rates.

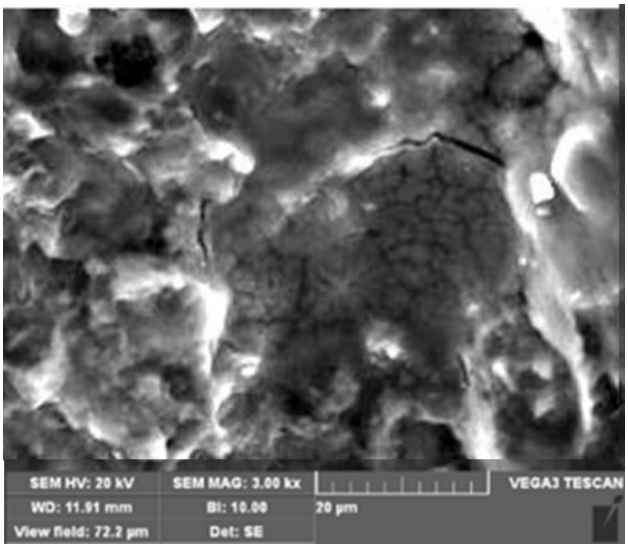

(a)

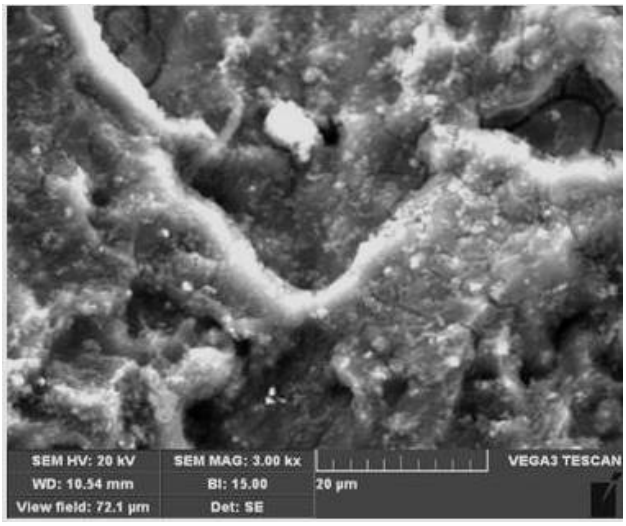

(b)

Figure 13 SEM images of sample surfaces: (a) near the fracture zone of the sample pre-deformed at the high strain rate; (b) near the fracture zone of the sample pre-deformed at the lower strain rate; The former shows more and larger micro-cracks than the latter.

To support the above discussion on the effect of strain rate on the ratio of the fraction of micro-cracks/voids to that of dislocations, X-ray diffraction analysis was conducted, since variations in dislocation density could be reflected by XRD peak broadening [86]. Figure 14 illustrates representative XRD patterns of the Mg alloy samples deformed at the two different strain rates. As shown, the XRD patterns of the samples, however, fail to show detectable variations in peak width. This may suggest that the difference in dislocation density between the samples experienced deformation at the high and low strain rates is not sufficient to show detectable difference in XRD peak width.

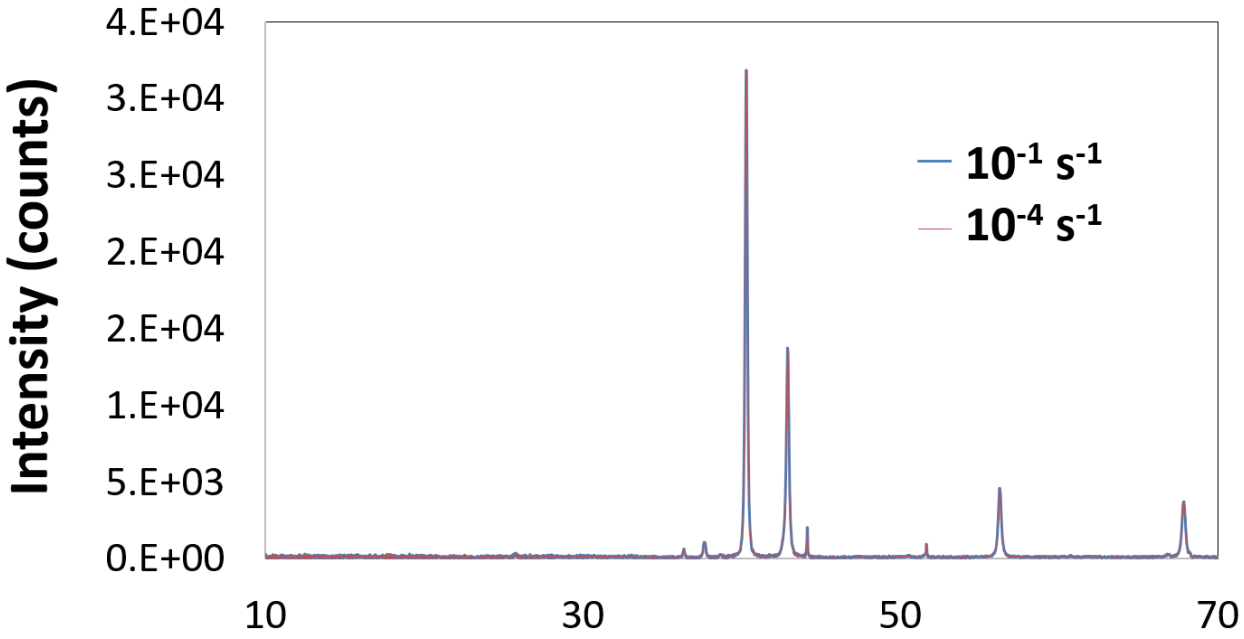

Figure 14 XRD pattern of Mg alloy samples deformed at the two different strain rates.

3.3.2 Variations in EWF with the strain rate

Allowing for the fact that work function is dependent on the electron density and sensitive to lattice distortion caused by defects[87], EWFs of the samples in different locations (corresponding to different strains) were measured using a Kelvin probe. Results of the measurements are illustrated in Figure 15. As shown, EWF is lowered as the strain increases when approaching the fracture surface. Such a decrease is primarily caused by plastic deformation with increased dislocation density, which renders the material more active. Micro-cracks/voids also decrease EWF, since they lower the density of material and consequently the electron density, on which EWF depends. The faster decrease in EWF of

the sample pre-deformed at the low strain rate, in which more dislocations and less micro-cracks/voids were generated, suggests that dislocations decrease EWF more rapidly or effectively than micro-cracks/voids.

One issue that needs to be clarified is that when more dislocations are introduced along with a decrease in EWF, hardness usually increases due to the strain-hardening effect. However, decreases in hardness were observed from locations 1 to 5, corresponding to successively increased strain. Such decreases are expected to be caused by formed micro-cracks/voids, which generate stress concentrations with which cracking is promoted. At the higher strain rate with more micro-crack/void generated during the deformation process, the decrease in hardness is larger as shown in Figure 12.

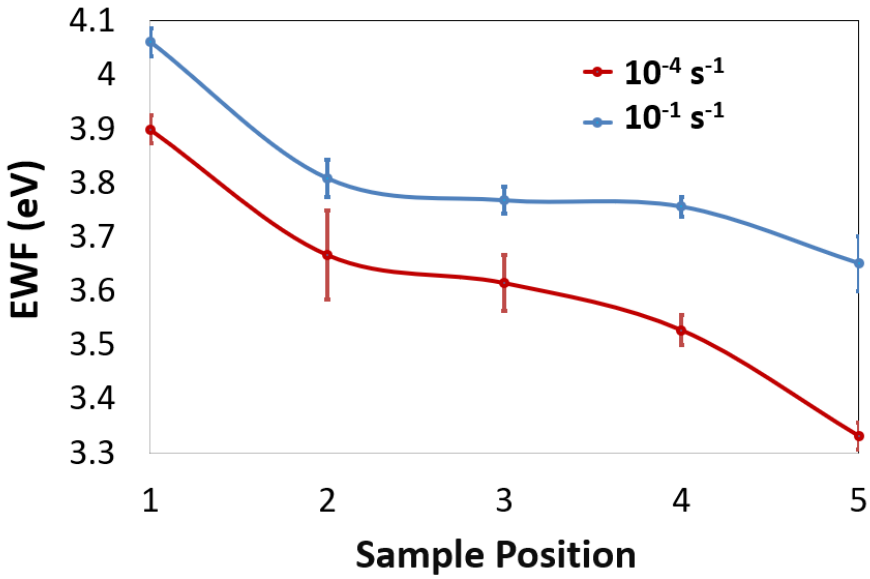

Figure 15 Variations in EWF of samples deformed at two different strain rates.

As mentioned earlier, it appears that dislocations decrease EWF more effectively than the micro-cracks/voids. To understand this issue, we may look into changes in electron density caused by deformation at high and low strain rates.

The local change in volume of the sample causes change in local electron density (the total number of valence electrons is constant). Changes in volume in different locations caused by deformation at the two strain rates, $10^{-1}s^{-1}$ and $10^{-4}s^{-1}$, were calculated based on the local dimensional changes caused by deformation. Figure 16 illustrates the regions where the volume changes were determined.

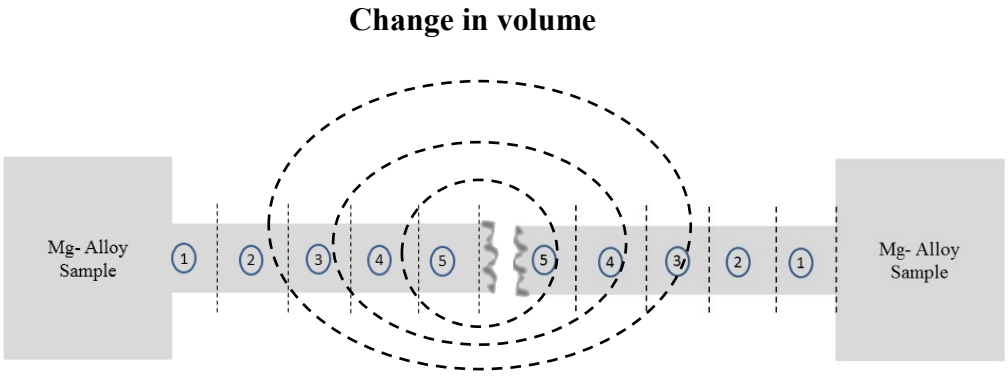

Figure 16 Volume changes of the regions were determined.

Calculated local changes in volume, $(V - V_0/V_0)$*100, caused by deformation at the two strain rates are given in Table 3. As shown, the low strain rate, at which more dislocations were generated, resulted in larger increases in volume. This may imply that dislocations

decrease the electron density more effectively than micro-cracks/voids, leading to larger decrease in EWF of the sample deformed at the low strain rate (Figure 15).

Table 3- Local changes in volume $(V\text{-}V_0/V_0)$ *100, caused by deformation at two strain rates

Volume change	**High strain rate** $(\boldsymbol{V - V_0})/\boldsymbol{V_0} * \mathbf{100}$	**Low strain rate** $(\boldsymbol{V - V_0})/\boldsymbol{V_0} * \mathbf{100}$
Position 5	7.64 %	19.47%
Position 3	4.15%	12.94%
Position 1	3.43%	10.69%

In order to further judge the above hypothesis, first-principle calculations were conducted to determine which type of defect, dislocation or vacancy cluster, results in a larger change in EWF.

Pre-relaxed models with the vacancy cluster and dislocation, respectively, were constructed as illustrated in Figure 17, which were used to generate relaxed systems containing vacancies and dislocations, respectively. As Figure 17(a) illustrates, four atoms (in blue) beneath the Mg-surface (MgSV) are removed; Figure 17(b) shows a dislocation beneath the Mg-surface after two atoms (in red) are removed (Mg_{SD}); Figure 17(c) Mg-surface with four atoms in

bulk (Mg_{BV}), which are apart away from the top surface, are removed to generate vacancies; and Figure 17(d) shows a dislocation in bulk (Mg_{BD}) after a row of atoms (in red) are removed. These systems are then relaxed to generate vacancies and dislocations as shown in Figure 18. Work functions of the surfaces were calculated using VASP, which equals the potential energy at vacuum level subtracting the Fermi level. Results of the calculation are presented in Figure 18(a). The calculation indicates that the vacancies and dislocations located near the surface result in surface distortion as shown in Figure 18(b) and Figure 18(c). The distorted surface caused by the dislocation in Mg_{SD} has a considerably lower work function than that caused by the vacancy cluster in Mg_{SV}. This is consistent with the experimental observation that the slowly deformed thick sample with more dislocations showed larger decrease in EWF than that of faster deformed samples with more vacancies or micro-voids (or vacancy clusters). However, when the vacancy cluster and dislocation are apart away from the surface, the difference in EWF is markedly smaller, since their influence on surface EWF is greatly reduced. Besides, the surface EWF becomes higher when atoms at the surface return to their relaxed positions as the defects are moved away from the surface. This is demonstrated by EWFs of MgBV and MgBD shown in Figure 18(a).

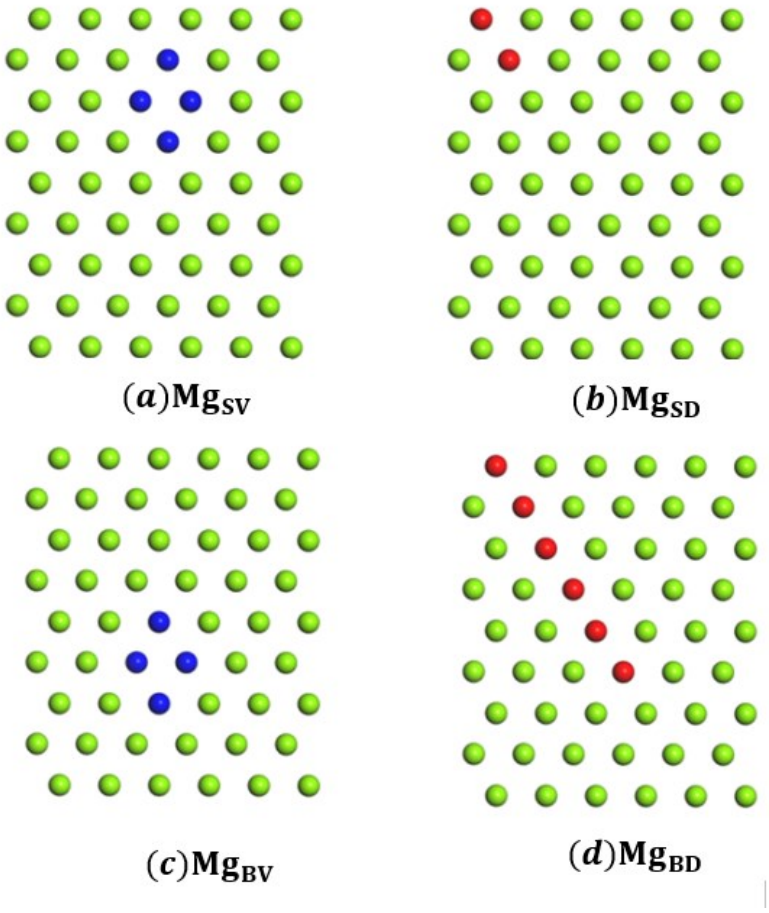

Figure 17 Pre-relaxed systems used to generate defects for calculating corresponding work functions. (a) four atoms (blue) beneath surface are removed to generate vacancies; (b) a dislocation is generated beneath the surface after two atoms (red) are removed; (c) A Mg-surface with four atoms in bulk, which are apart away from the top surface, are removed to generate vacancies; and (d) a dislocation is generated in bulk after a row of atoms (red) are removed. Note: these systems need to be relaxed in order to generate the defects.

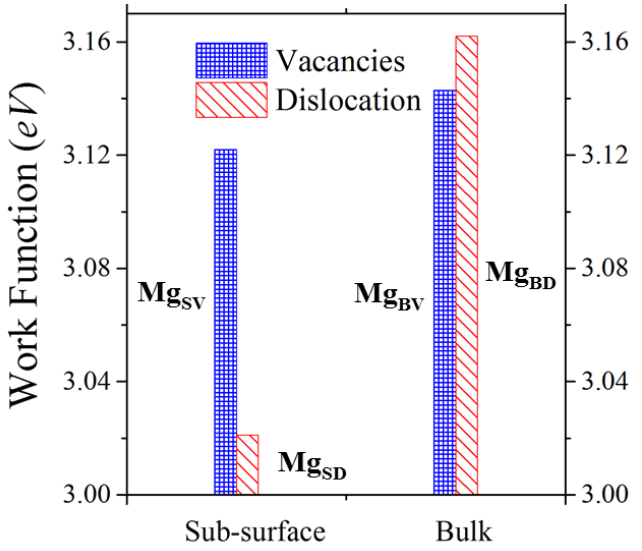

(a)

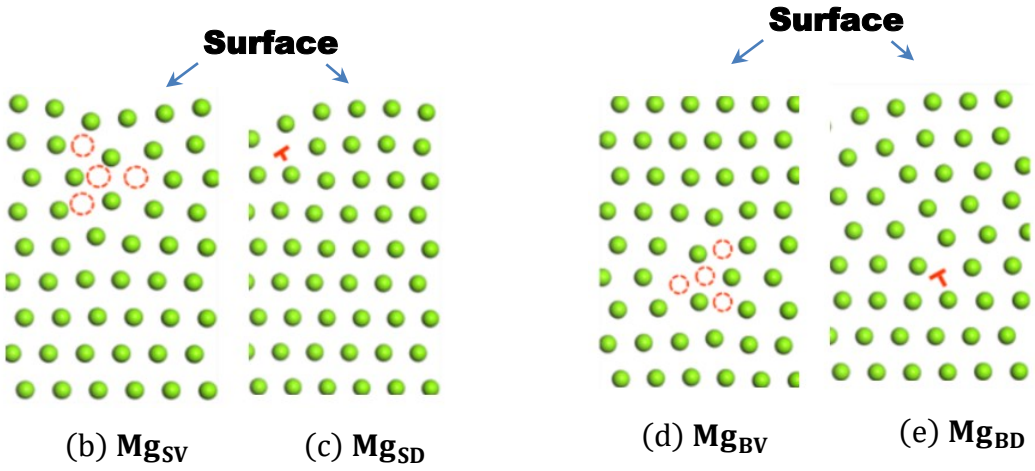

(b) **Mg_{SV}** (c) **Mg_{SD}** (d) **Mg_{BV}** (e) **Mg_{BD}**

Figure 18(a) Electron work functions of relaxed surfaces on systems (b – e) calculated with VASP; (b) a system having vacancies near the top surface (Mg_{SV}), (c) a system having a dislocation near the top surface (Mg_{SD}); (d) a system having vacancies apart away form the top surface (Mg_{BV}); and (e) a system having a dislocation apart away from the top surface (Mg_{BD}).

3.3.2.1 Wear resistance

Wear resistances of samples deformed at the low and high strain rates, respectively, were evaluated. Figure 19 illustrates volume losses of the samples measured in different locations, which are consistent with local hardness. The sample deformed at the low strain rate with the formation of more dislocations but fewer micro-cracks/voids is harder than that deformed at the higher strain rate. Correspondingly, the former showed smaller volume loss than the latter during the wear test. The samples deformed respectively at the high and low strain rates did not show large difference in the friction coefficient as Figure 20 illustrates. However, due to considerably decreased hardness with many more micro-cracks/voids, the frictional coefficient measured in the location near the fracture surface is distinctively larger than those in other locations.

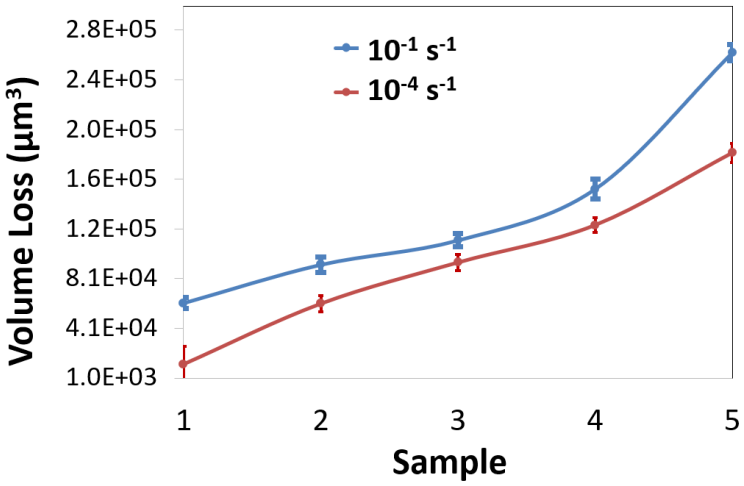

Figure 19 Volume losses of the samples in different locations. The one deformed at the high strain rate shows a lower resistance to wear than that deformed at the lower strain.

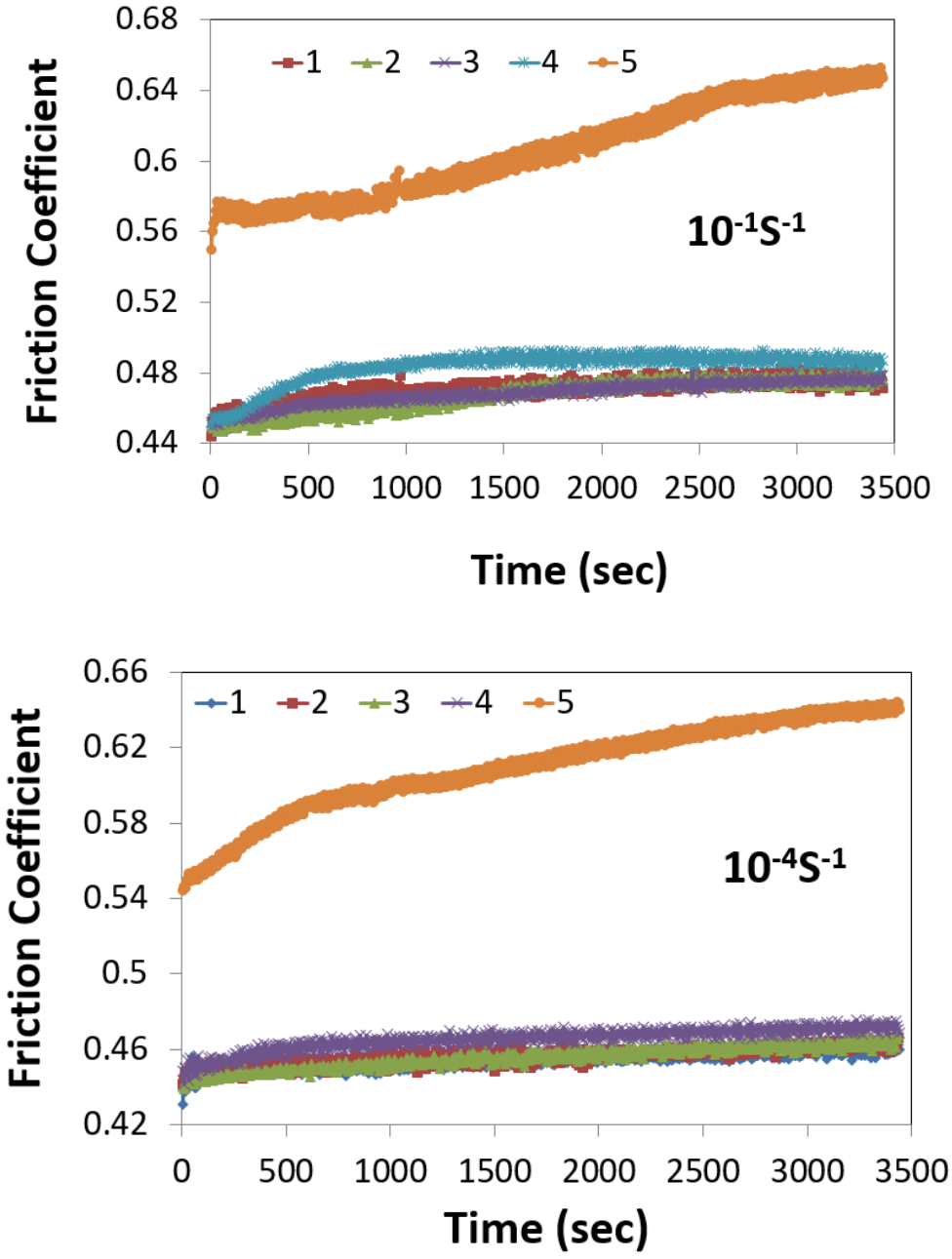

Figure 20 Friction coefficient vs. sliding time in different positions of the samples deformed at the two different strain rates.

SEM observation and corresponding EDS analysis were carried out on wear tracks near the fracture zone as shown Figure 21. Quantified data of the EDX analysis is provided in Table 4 and Table 5 respectively.

Table 4 EDS characterization showing oxygen content at various position for slow strain rate sample

Sample ($10^{-4}s^{-1}$)	% Mass	
	Oxygen(O)	Magnesium (Mg)
Spot 1	28.43204	65.6032
Spot 2	0.551258	77.53178

Table 5 EDS characterization showing oxygen content at various position for fast strain rate sample

Sample ($10^{-1}s^{-1}$)	% Mass	
	Oxygen(O)	Magnesium (Mg)
Spot 1	38.16722	53.69532
Spot 2	0.815354	77.13975

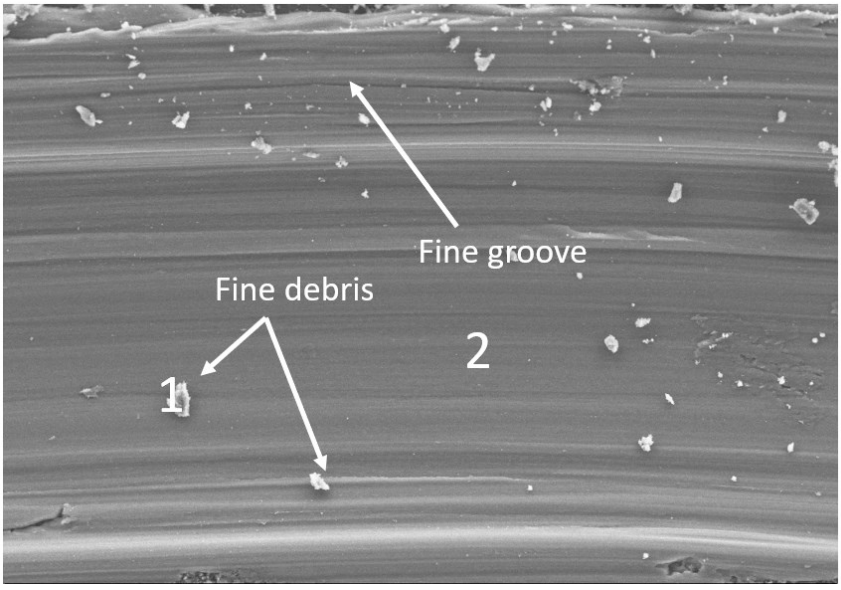

(a)

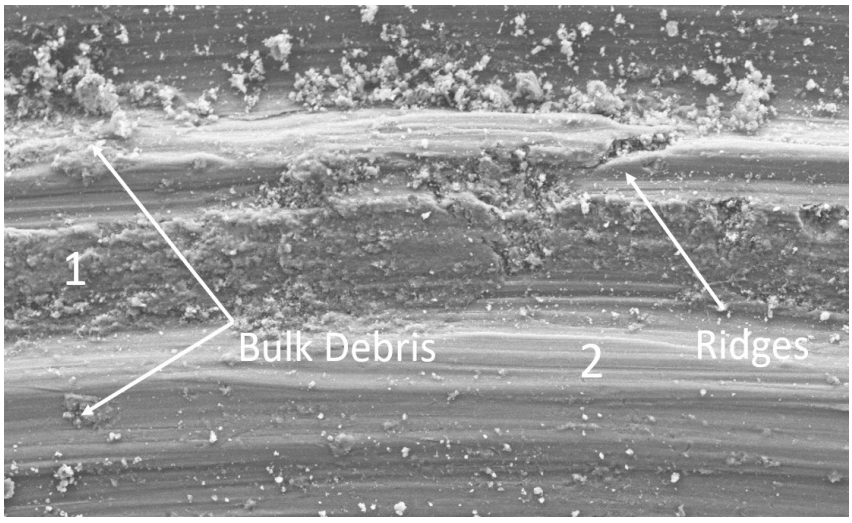

(b)

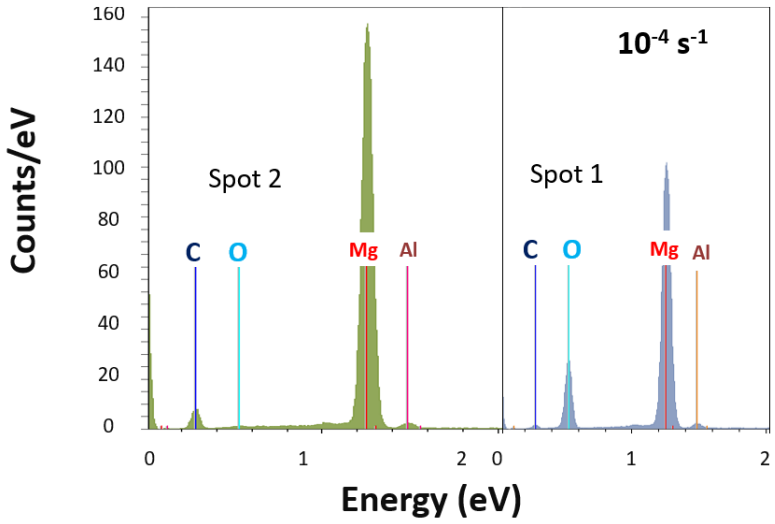

(c)

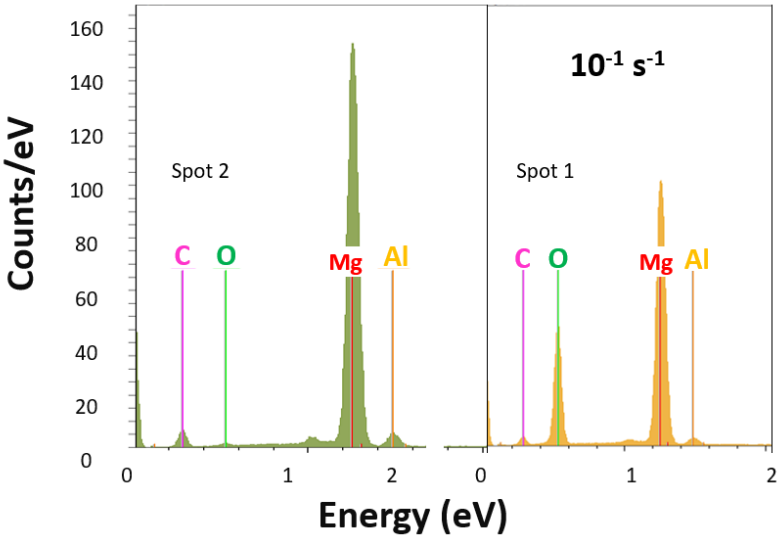

(d)

Figure 21 SEM and EDS of the dry wear track on AZ31 samples; (a) SEM image of the sample pre-deformed at the low strain rate, (b) SEM image of the sample pre-deformed at the higher strain rate; (c) EDS of the sample pre-deformed at the low strain rate, (d) EDS of the sample pre-deformed at the higher strain rate.

Figure 21 shows wear tacks of the samples with ridges and grooves along the sliding direction. The morphology of the wear tracks show the features of abrasive wear, in which plough into the sample surface, causing material loss by removal of small fragments so ribbon-like chips of material. It is clear that the sample pre-deformed at the high strain rate had considerably more wear debris than that pre-deformed at the lower strain rate due to the fact that more microcracks/voids were formed at the high strain rate. As Figure 21(b) illustrates, the worn surface of the sample pre-deformed at the high stratin rate shows poor surface integrity resulting from micro-cracks/voids.

Figure 21(c) and (d) shows the spectra of EDS analysis. Data collected at spot1 and spot 2 represent compositions of the wear debris and the worn area. As shown, the wear debris contains more oxygen, impllying that oxidation more or less occurred on the wear track during the wear tests.

3.3.3 Corrosive wear

The performances of the samples pre-deformed respectively at the low and high strain rates during wear in tap water were evaluated in order to evaluate the effect of the strain rate on corrosive wear of the deformed Mg alloy samples. During corrosive wear, material degradation is increased by defects introduced during the pre-deformation. The defects made the samples more anodic with raised corrosion rate, thus accelerating wear [84-85].

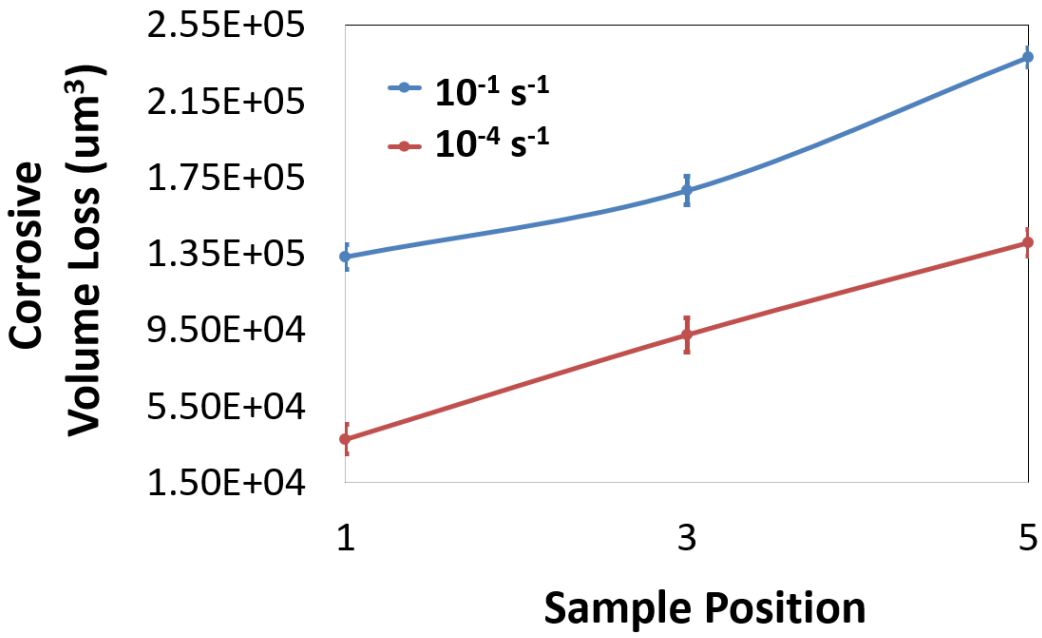

Figure 22 Volume loss of the samples at different locations during the corrosive wear test. The sample pre-deformed at the higher strain rate shows more volume loss than that deformed at the low strain rate.

As shown in the next section, the sample pre-deformed at the lower strain rate (introduced more dislocations) was corroded faster than that pre-deformed at the high strain rate. The raised dislocation density by deformation can increase the corrosion rate, which enhances the wear-corrosion synergy and leads to faster material dissolution.

Figure 22 illustrates volume losses of samples pre-deformed at the high and low strain rates. As shown, the higher strain rate still resulted in more wear, indicating that mechanical damage played a predominant role in causing wear of the samples in the aqueous solution. The pre-existing micro-cracks could act as stress raisers and made the surface vulnerable to wear

attack, especially in a corrosive environment. The stress concentration at the crack tip may render the local region more active [14], promoting local corrosion and thus leading to accelerated crack propagation.

Figure 23 illustrates SEM micrographs and EDS spectra of wear tracks near the freacture zone for the AZ31 Mg samples after the wear test in tap water. One may see that the wear track on the sample pre-deformed at the high strain rate had many microcracks, compared to that on the sample pre-deformed at the lower strain rate. In addition, during the corrosive wear tests, more microcracks were formed, compared to the situation of dry wear tests, implying that wear-corrosion synergy promoted fracture or cracking when corrosion was involved. The pre-deformation at the higher strain rate further promoted such failure mode.

Table 6 EDS characterization of corrosive wear showing oxygen content at various position for slow strain rate sample

Sample ($10^{-4}s^{-1}$)	% Mass	
	Oxygen(O)	Magnesium (Mg)
Position 1	52.57913	17.46773
Position 2	8.956576	52.45395

Table 7 EDS characterization of corrosive wear showing oxygen content at various position for fast strain rate sample

Sample ($10^{-1}s^{-1}$)	% Mass	
	Oxygen(O)	Magnesium (Mg)
Position 1	59.11794	25.73809
Position 2	3.687496	72.17633

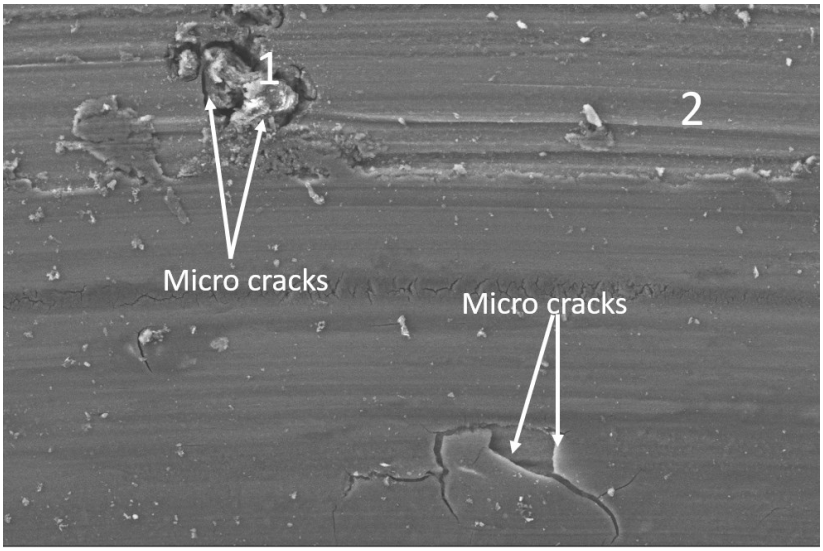

(a)

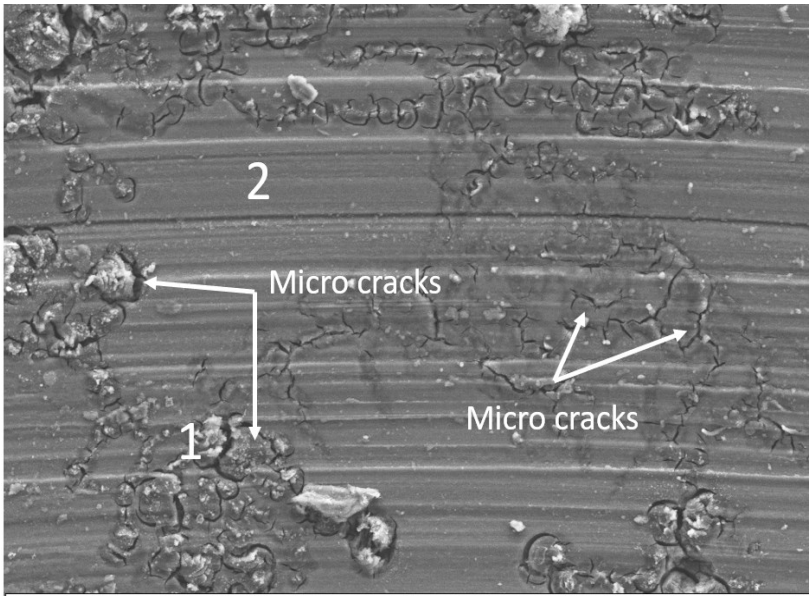
2
Micro cracks
1
Micro cracks

(b)

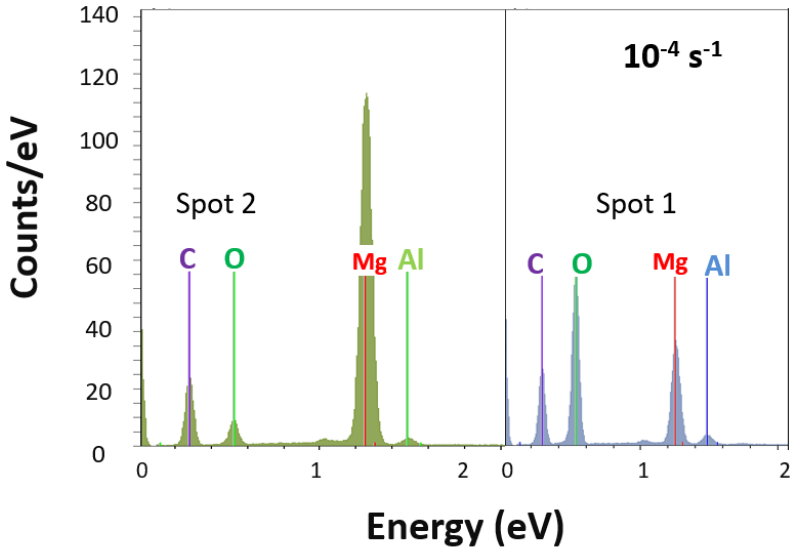
140
120
100
80
60
40
20
0
Counts/eV
Spot 2
C
O
Mg
Al
Spot 1
C
O
Mg
Al
10-4 s-1
0
1
2
0
1
2
Energy (eV)

(c)

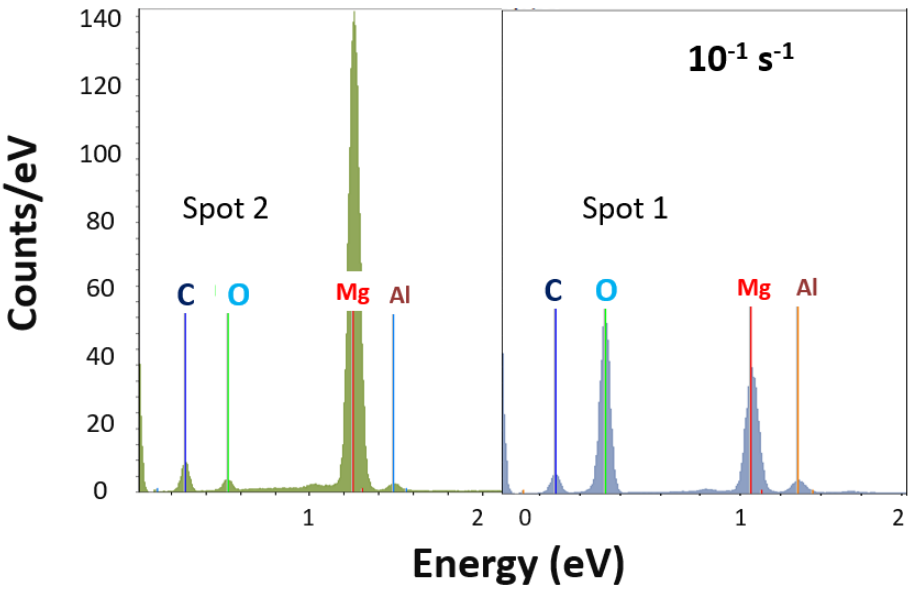

(d)

Figure 23 SEM and EDS of the corrosive (wet) wear tracks on AZ31 samples; SEM image of the sample pre-deformed at the low strain rate, (b) SEM image of the sample pre-deformed at the higher strain rate; (c) EDS of the sample pre-deformed at the low strain rate, (d) EDS of the sample pre-deformed at the higher strain rate.

Figure 23(a) and Figure 23(b) depict the EDS spectra of the samples in spot 1 and 2. Corresponding values of the various elements are given in tables 3 and 4, respectivelty. As shown, more oxidation was involved when tested in the corrosive environment, although the corrosivity of tap water was not high.

3.3.4 Corrosion

The corrosivity of tap water to the Mg alloy was also evaluated in order to better understand the performance of the samples during the corrosive wear tests (solution: tap water). The corrosion behavior of the deformed samples was evaluated through immersion tests. Average weight loss rates of positions 1~ 5 for the sample after being immersed in the solution for different durations, 30 min, 60 min, and 120 min were determined. Average corrosion rates in different locations are illustrated in Figure 24. As shown, the sample deformed at the low strain rate was corroded faster than that deformed at the higher strain rate. This suggests that the deformed sample with more dislocations or higher fraction of dislocation to micro-crack/void is corroded faster than the one with fewer dislocations. The measured corrosion rates of the samples are consistent with their EWFs. As shown in Figure 15, the EWF of sample deformed at the lower strain rate is lower than that of the sample deformed at the high strain rate, meaning that the former is electrochemically more active than the latter. This explains the difference in corrosion rate between the samples deformed at the low and higher strain rates.

In terms of corrosive wear, though the corrosion rate of the sample deformed at the high strain rate is smaller than that deformed at the lower strain rate, the larger volume loss of the former indicates that the micro-cracks/voids are more detrimental to the Mg alloy when it encounters wear in the aqueous solution.

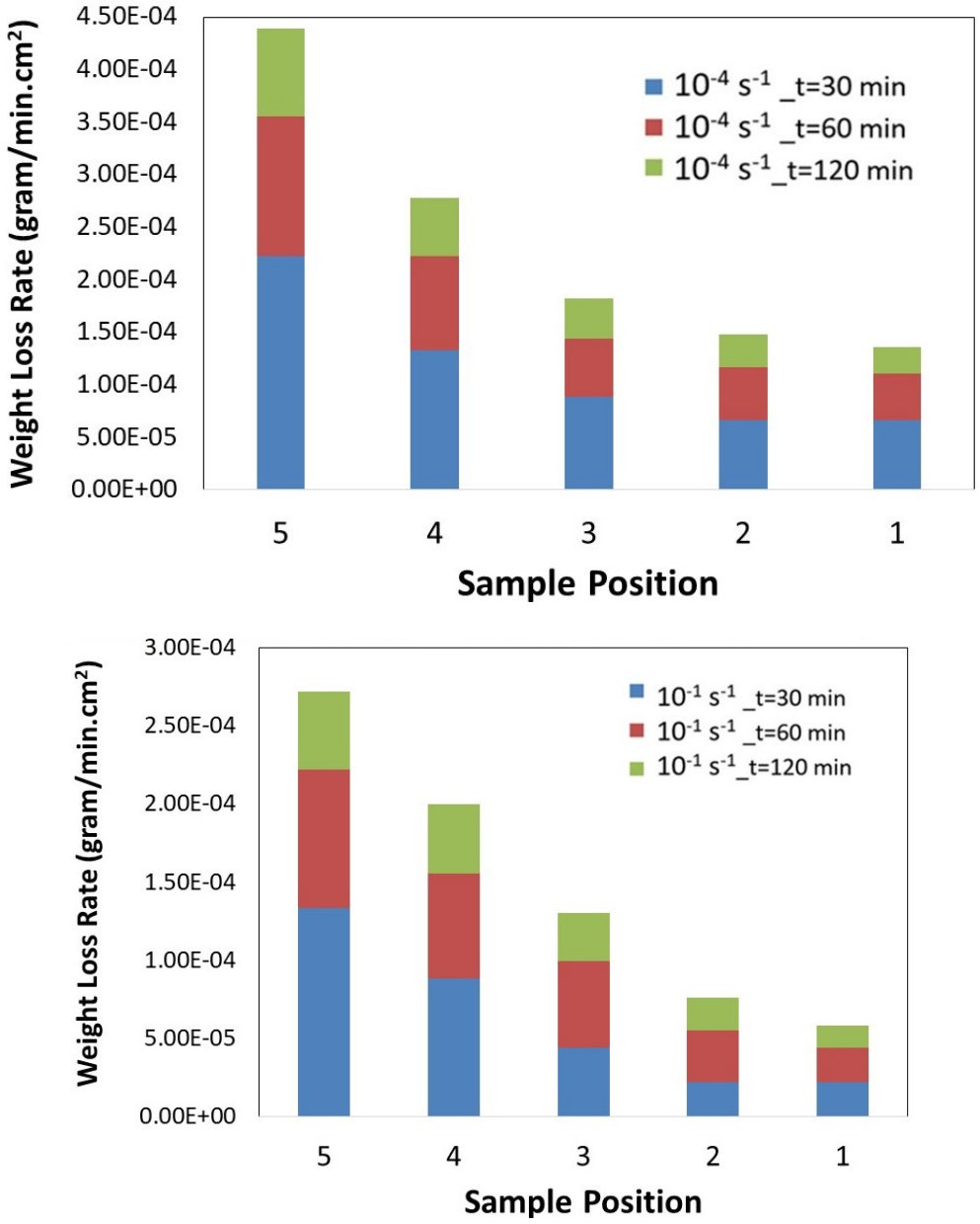

Figure 24 weight loss rate (gram/min.cm^2) of the samples at different locations during corrosion testing.

It was noticed that the weight loss rate varied with the immersion time. This may be ascribed to the formation of an oxide scale on the samples. During immersion tests, dissolution and formation of a porous oxide scale occurred simultaneously in the aqueous solution. The oxide scale, though porous, could slow down the dissolution of the alloy as the immersion time was prolonged. When the immersion time continuously increased, the process of simultaneous oxide scale development and material dissolution would become stable. As a result, the difference in the weight loss rate would become smaller and eventually negligible.

When wear occurred in the tap water, though the corrosion rate of the sample deformed at the higher strain rate was smaller than that deformed at the low strain rate, the larger volume loss of the former caused by corrosive wear may indicate that the micro-cracks/voids are more detrimental to the Mg alloy when worn in the aqueous solution, whose corrosivity is not high.

3.4 Conclusions

Influences of pre-deformation at two strain rates, $10^{-4}/s$ and $10^{-1}/s$, on hardness, electron work function, wear resistance, corrosion, corrosive wear of AZ31 alloy were investigated.

(1) It was observed that the hardness of deformed samples decreased with an increase in the strain magnitude, ascribed to the formation of micro-cracks/voids, which consequently affected the wear resistance. The deformation at the lower strain rate resulted in smaller decrease in hardness than that at the higher strain rate corresponding to the high wear resistance.

(2) XRD diffraction analysis did not provide clear clues in regard to the residual strain, which is related to the dislocation density. However, the measured electron work function (EWF) showed that the lower strain rate led to a larger decrease in EWF, associated with a higher ratio of the fraction of dislocations to that of micro-cracks/voids, corresponding to higher surface activity and lower corrosion resistance.

(3) Although the micro-cracks/voids less deteriorated the corrosion resistance, they considerably weakened the material against wear. As a result, samples experienced deformation at the higher strain rate showed a lower resistance to corrosive wear. These are explainable based on measured EWFs. The conducted first-principle calculations support the explanations.

(4) This study also shows that the work function can provide supplementary information that helps understand the underlying mechanisms for the observed phenomena.

CHAPTER 4

4. Effect of strain rate and sample thickness of brass

We investigated influences of these two factors; strain rate and sample thickness, on hardness of deformed thin brass sheets and consequently their wear behavior. It was observed that a lower strain rate caused smaller decrease in hardness than the higher strain rate for a sheet of one mm in thickness. However, the situation was reversed for a thinner sheet, leading to different variations in the wear behavior. The objectives of this study are 1) to investigate and understand influences of strain rate and sample thickness on strain-softening of deformed brass thin sheets and corresponding wear behavior, and 2) evaluate the usefulness of work function as a potential parameter in understanding the defect-involved mechanical state of materials.

4.1 Experimental method

Samples of annealed brass thin sheets with two different thicknesses, 0.4 mm and 1.0 mm, were used for the study. Tensile deformation was applied to the samples at two strain rates,

$10^{-4}s^{-1}$ and$10^{0}s^{-1}$, respectively, using an Instron machine. The sample gauge length is 80 mm. Samples deformed under different conditions are denoted as

THIN(-4): thin sample (0.4 mm) deformed at the low strain rate of $10^{-4}s^{-1}$

THIN(0): thin sample (0.4 mm) deformed at the high strain rate of $10^{0}s^{-1}$

THIC(-4): thick sample (1.0 mm) deformed at the low strain rate of $10^{-4}s^{-1}$

THIC(0): thick sample (1.0 mm) deformed at the high strain rate of $10^{0}s^{-1}$

Strains in different locations along the sample's longitudinal axis were determined based on distortion of grids which were marked on the samples. Sample surface was lightly polished using SiO_2 sand papers and cleaned using an ultrasonic cleaner with reagent alcohol. Hardness was determined with a micro-indenter made by Fischer Technology Inc. (Windsor, CT, USA). Reported hardness values are averaged over at least five measurements with standard deviation around 10-15%. The zones near the fractured area and those about 10 mm away from the fractured area were observed (after etching using dilute ammonium hydroxide) under a scanning electron microscope. X-ray diffraction patterns of the zones near the fractured area were obtained with an XRD system (D8 DISCOVER, Bruker). EWFs in different locations were measured using a scanning Kelvin probe (KT Technology, UK)[90]. Reported EWF values are averaged over 10 measurements. Wear tests were performed on a pin-on-disc wear tribometer (CSEM Instruments, Neuchatel, Switzerland) at room temperature (20°C). The disc was the sample under study and the pin was a silicon nitride ball with 6 mm in diameter. All tests were performed at a sliding speed of 0.5 cm/s along a circular path of 2.0 mm in

diameter under a normal load of 5 N for a sliding distance of 18 m. Wear tracks and corresponding volume losses of the samples were determined using a confocal microscope (ZeGage 3D optical profilometer, Zygo Corp.). At least three tests were performed for each reported wear loss value.

4.2 Results and discussion

4.2.1 Variations in hardness with the strain rate and sheet thickness

Figure 25 illustrates hardness values measured in different locations from the central fractured area to the place close to the sample end. The strain is larger in the central area and decreases with the distance from the central area. As shown, hardness decreases when approaching the central area with larger strain. For the thick sheet (thickness=1.0 mm) deformed at the high strain rate, its hardness is lower than that of the sample deformed at the lower strain rate. However, for the thin sheet (thickness=0.4 mm), the trend is reversed.

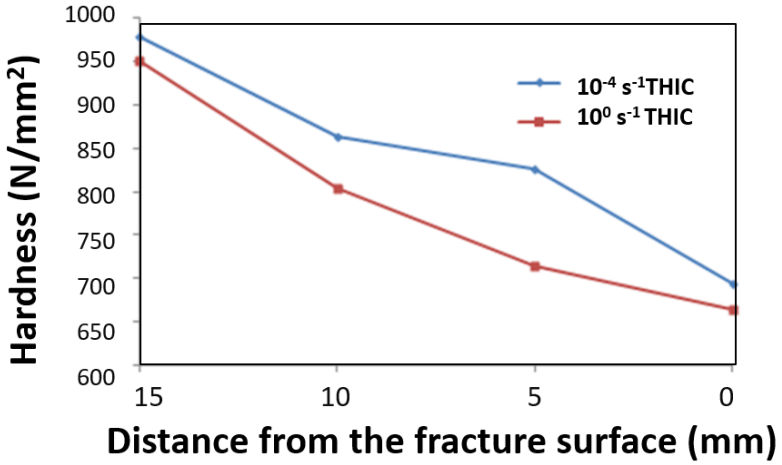

(a)

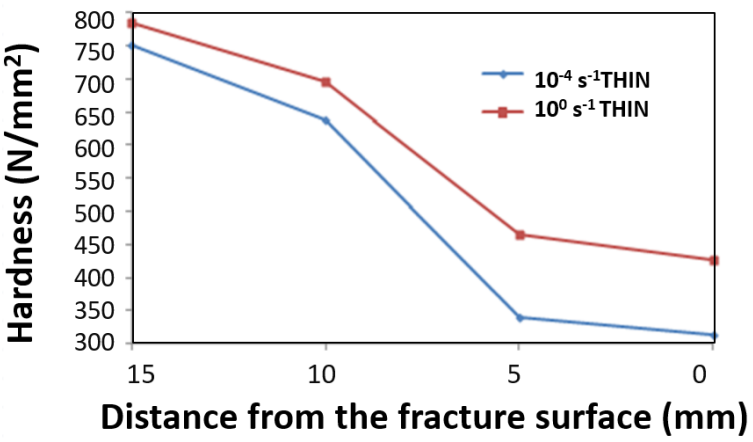

(b)

Figure 25 Hardness values measured in different locations from the central fractured area to the place closer to the sample end. (a) thick sheet, and (b) thin sheet. The fracture surface is in the sample's central area where fracture occurred. The reported hardness values are averaged over at least five measurements with standard deviation around 10-15%.

When occurring in a crystal lattice, the dislocation movement may obey Newton's law of motion[54] :

$$\vec{f} = m * (\frac{\partial \vec{V}}{\partial t})$$

where $\vec{f}$ is the force required to drive the dislocation to move in the crystal lattice, and $(\partial \vec{V} / \partial t)$ is the acceleration for the dislocation to reach a certain speed.

There must be a drag force on the dislocation before a certain velocity is reached. The drag force rises as the dislocation is generated and driven at a higher strain rate, corresponding to a larger equivalent mass. Thus, at high strain rates, dislocations are less easy to be generated and moved. Consequently, formation of micro-voids or clusters of vacancies and micro-cracking is promoted in order to accommodate deformation, leading to a larger decrease in hardness. Besides, more micro-voids are generated with increasing strain at the high strain rate. This explains why hardness of the thick sheet deformed at the high strain rate is lower than that deformed at the lower strain rate, as shown in Figure 25 (a). However, it should be indicated that the present high strain rate ($10^0 s^{-1}$) is not very high and corresponding dislocation velocity could not be large enough to markedly affect m* and thus the dislocation density. Nevertheless, the lowered hardness of the sample deformed at the higher strain rate could be explained based on the dislocation dynamics, though is difficult to make quantitative analysis, bearing in mind that the dislocation velocity is not only related to the strain rate but also the density of moving dislocations [91].

The situation is reversed for the thin sheet of 0.4 mm in thickness i.e., the lower strain rate resulted in greater decrease in hardness (see Figure 25 (b)). A possible reason is that, in the thin sheet with less lattice confinement, dislocations generated at the low strain rate may migrate to the surface and vanish in order to reduce the strain energy caused by dislocations [92]. However, at the high strain rate, generated dislocations inside the sample with larger equivalent mass more slowly. Besides, less lattice confinement could promote dislocation generation in contrast with the formation of cracks or micro-voids to accommodate

deformation. These may lead to smaller decreases in hardness of the thin sheet deformed at the high strain rate.

4.2.2 XRD analysis and SEM observation

In order to confirm the above hypotheses, X-ray diffraction analysis was conducted. Since the strain rate may alter dislocation density and formation of micro-voids, the residual strain may be different, which could be reflected by XRD peak broadening. Figure 26 illustrates representative XRD patterns of the thin and thick sheets deformed at different strain rates. The analyzed area is close to the central zone of the samples. As illustrated, the XRD patterns of these samples are overlapped and do not show distinguishable variations in peak width. This may suggest that the difference in density of dislocations generated under the current conditions is not sufficient to result in detectable difference in XRD peak width.

To obtain more information, the samples were examined under the scanning electron microscope. Figure 27 illustrates etched sample surfaces. As shown, micro-voids or clusters of vacancies exist not only in the area near the fracture surface but also in locations apart away from the area. The micro-voids or vacancy clusters may relax the distorted lattices and thus minimize the broadening of XRD peaks caused by residual stress or strain.

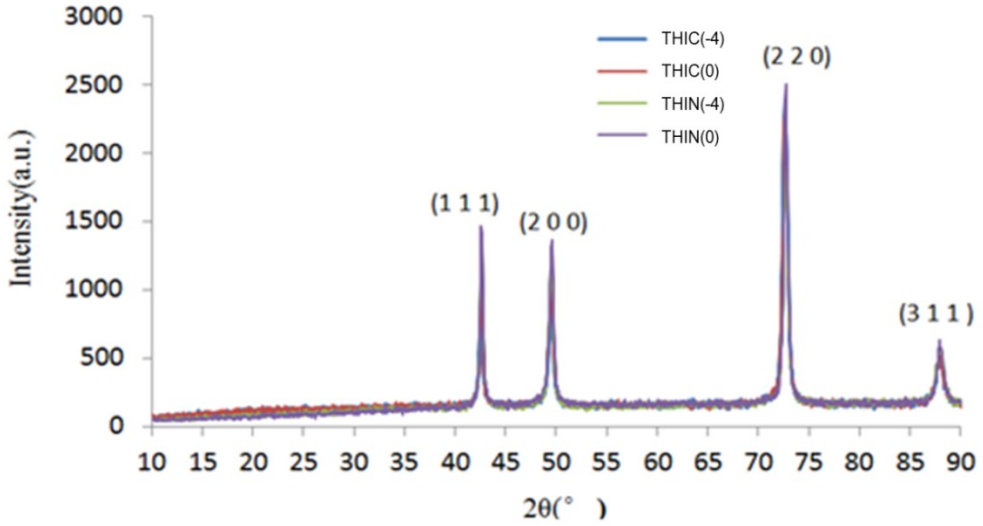

Figure 26 XRD patterns of thin and thick sheets deformed at different strain rates

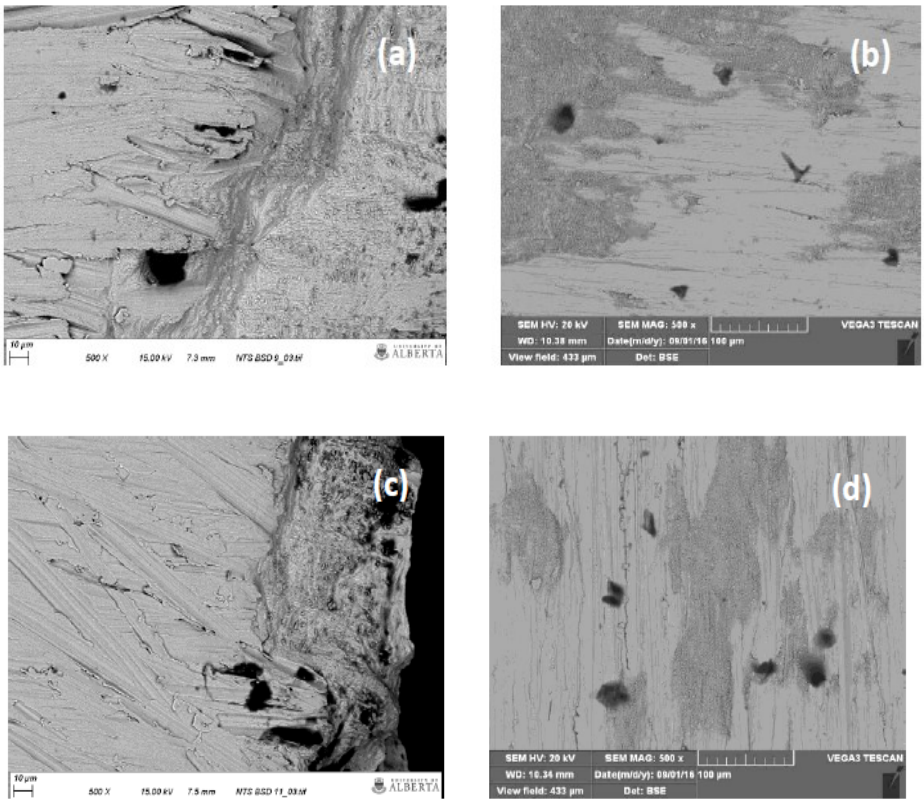

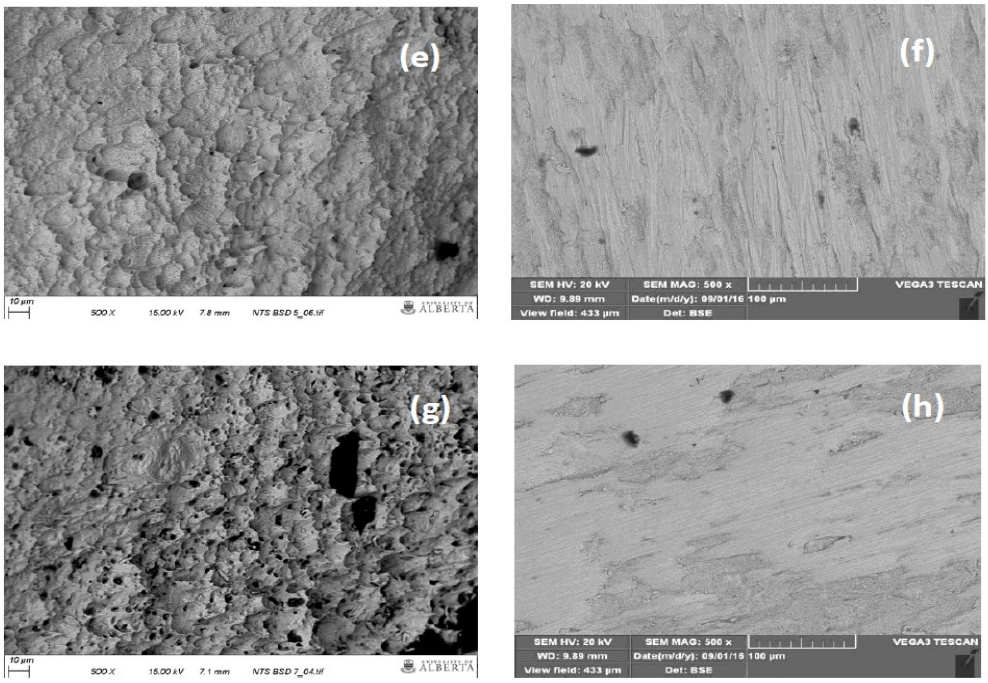

Figure 27 SEM images of sample surfaces: (a) near the fracture zone of THIN(-4); (b) about 10 mm away from the fracture zone of THIN(-4); (c) near the fracture zone of THIN(0); (d) about 10 mm away from the fracture zone of THIN(0); (e) near the fracture zone of THIC(-4). The insert gives a closer view of micro-voids; (f) about 10 mm away from the fracture zone of THIC(-4); (g)) near the fracture zone of THIC(0); (h) about 10 mm away from the fracture zone of THIC(0).

It is clear that the strain-softening of the brass thin sheets is ascribed to the formation of micro-voids or vacancy clusters, which reduce the load-bearing capability. Since dislocations generally result in strain hardening due to dislocation mutual interactions, the degree of the

observed strain-softening should be related to the ratio of micro-voids to dislocations, which is influenced by the strain rate and sample thickness. For the thick sample, the high strain rate resulted in more micro-voids than the lower strain rate, leading to lower hardness. However, for the thin sample, due to the lower lattice refinement, micro-voids could be generated with ease and at the low strain rate the dislocations could migrate to the sample surface and vanish, thus making the sample deformed at the low strain rate softer than that deformed at the higher strain rate (dislocations stay inside the sample and accommodate deformation). However, it is difficult to obtain information on the ratio of micro-voids to dislocations in order to quantitatively support the above argument.

4.2.3 Variations in EWF with the strain rate and sample thickness

EWFs in different locations were measured using a Kelvin probe. Figure 28 illustrates variations in EWF with strain for both the thick and thin samples deformed at the high and low strain rates, respectively. As shown, EWF is lowered as the strain increases. Such a decrease was caused by lattice distortion or deformation with increased dislocation density, which rendered the material more active. Formation of micro-voids or vacancy clusters during deformation decreased EWF as well, since they also caused lattice distortion and reduced the electron density on which EWF depends.

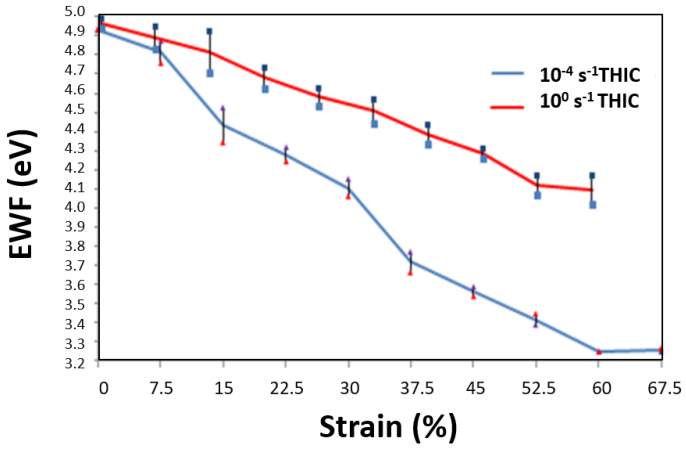

(a)

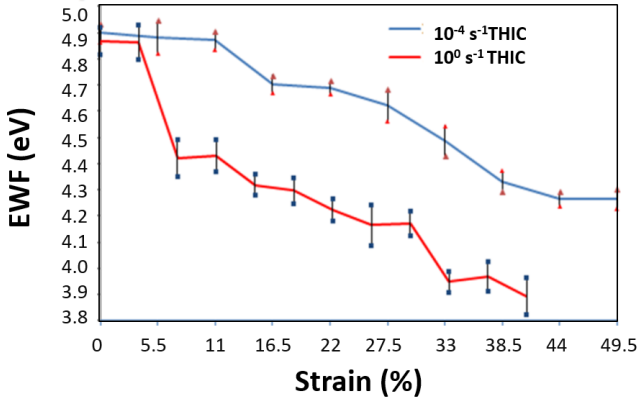

(b)

Figure 28 variations in EWF with strain of (a) thick samples and (b) thin samples deformed at the high and low strain rates, respectively.

However, trends of variations in EWF of the thick and thin samples with increasing strain are different, which are summarized below with possible mechanisms:

(a) For thick samples deformed at the low strain rate, their EWF decreased with strain faster

than that of those deformed at the higher strain rate. This should result from more dislocations generated at low strain rate, while less dislocations but more micro-voids were introduced at the higher strain rate.

(b) For the thin samples, EWF of samples deformed at the high strain rate decreased faster than that of those deformed at the low strain rate. At the high strain rate, generated dislocations have larger equivalent mass and are less easy to move to the surface where they could vanish. However, at the low strain rate, dislocations could be relatively easier to move to the surface in order to reduce the strain energy, leading to smaller decreases in EWF.

(c) The changes in EWF are consistent with the changes in hardness. One issue that needs to be clarified is that when more dislocations are introduced along with a decrease in EWF, the dislocation interaction should result in the strain-hardening effect. However, for thin metal sheets, deformation is achieved by both plastic deformation and generation of vacancy clusters or micro-voids. The latter deteriorates the structural integrity and causes stress concentration under external loads, thus reducing the stress-bearing capability and resulting in strain-softening.

One more issue worth being confirmed is related to the effects of dislocation and micro-voids on work function. As Figure 25(a) and Figure 28(a) illustrate, more micro-voids and less dislocations were generated in the thick sample deformed at the higher strain rate. The observed changes in work function and hardness imply that dislocations lead to larger

decreases in work function than micro-voids or vacancy clusters.

4.2.4 Wear resistance

The strain-softening caused by micro-voids would deteriorate materials' resistance to failure. In this study, we evaluate resistances of the samples to wear for further confirmation. For each sample, four locations from a zone near the fracture surface to one close to the sample end were tested. Figure 29 shows volume losses of the samples measured at different locations.

The observed wear behavior of the samples is consistent with their hardness. For the thick samples, the one experienced deformation at the lower strain rate is harder with less micro-voids than that deformed at the higher strain rate. As a result, the former shows smaller volume loss than the latter during the wear test. For thin sample, zone near the fracture surface, there is no difference in wear loss between samples deformed at high and low strain rates, since high density micro-voids in this zone significantly increased crack nucleation and propagation during the wear tests. For thick samples, the one deformed at the higher strain rate shows a lower resistance to wear than that deformed at the low strain rate; while for the thin samples, the difference in volume loss was not significant. The one experienced at the higher strain rate is harder than the one deformed at the low strain rate, leading to decreased material loss during the wear test, though the decrease in volume loss is slight. This could be ascribed to their low hardness and less lattice confinement for micro-void formation during the deformation process, compared to those of the thick samples. This may minimize the

difference in their resistances to wear when comparing the performances of thin samples deformed respectively at high and low strain rates.

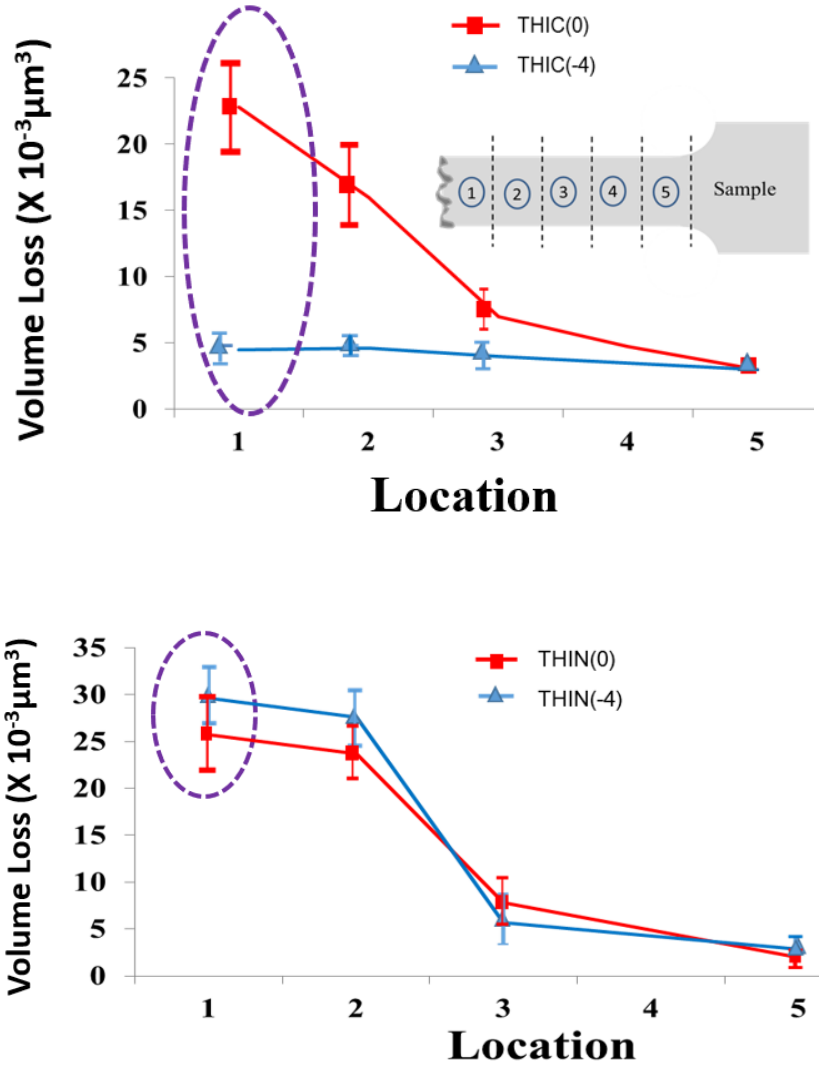

Figure 29 Volume losses of the samples caused by wear in different locations.

Worn surfaces of the samples were observed under a scanning electron microscope. Figure 30 illustrates worn surfaces tested in region 1 near the fracture surface. For the thick samples, the one deformed at the high strain rate shows more micro-cracks than the one deformed at the lower strain rate. The higher density of micro-voids in the former should be responsible for the promoted micro-cracking due to raised stress concentration. For the thinner samples, the worn surface appearances of the samples deformed at high and low strain rates do not show large difference and both depict micro-cracks.

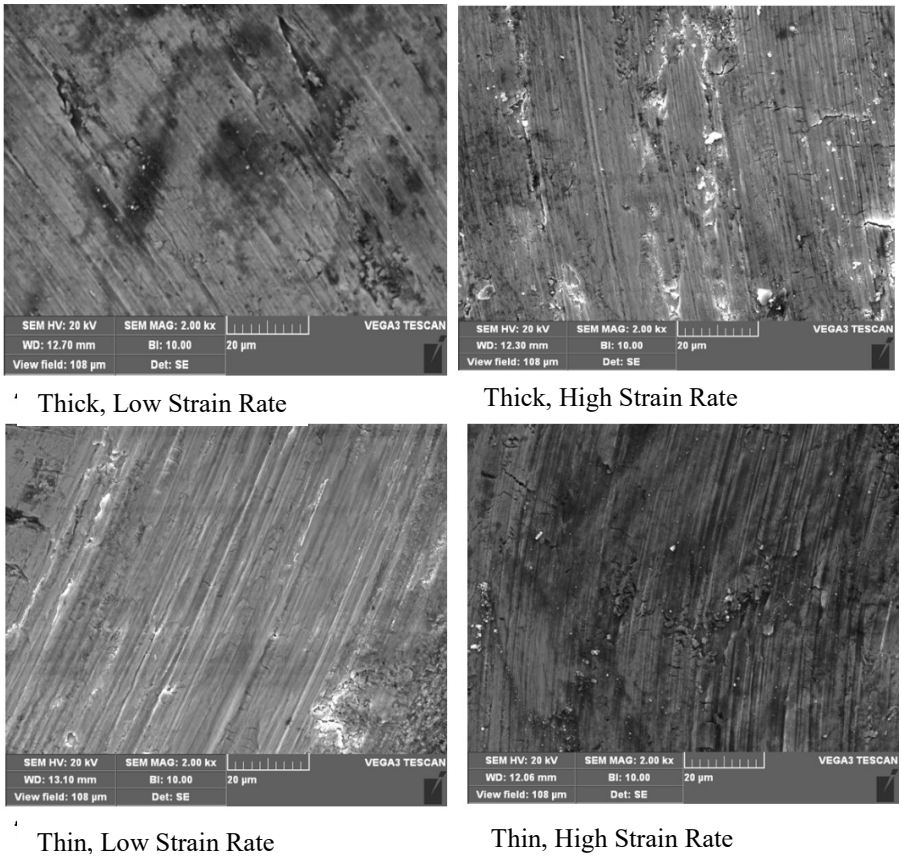

Figure 30 Worn surfaces tested in the area (region 1) near the fracture surface.

4.3 Conclusions

Effects of strain rate on hardness and wear resistance of deformed brass sheets with two different thicknesses, 1.0 mm and 0.4 mm, were investigated.

(1) Instead of strain-hardening, hardness of the sheets decreased with an increase in the strain magnitude, ascribed to the formation of micro-voids, which consequently affected the wear resistance.

(2) The deformation at a lower strain rate resulted in a smaller decrease in hardness than that at the higher strain rate for the thick sheet. However, the situation was reversed for the thin one, which is ascribed to the relative ease for dislocations to migrate to the sample surface and vanish there, thus reducing the decrease in hardness, of the thin sample.

(3) XRD diffraction analysis did not give clear clues in regard to residual strain or dislocation density but the measured electron work function helps explain the observed phenomena.

(4) The wear testing demonstrates that the strain rate has negligible effect near the fracture area position of the sample because of crack nucleation and propagation during the wear tests caused by high density micro-voids.

CHAPTER 5

5. General conclusions and future work

5.1 General conclusions

In this thesis study, effects of strain rates and thickness on hardness, wear resistance, corrosive wear and corrosion of pre-deformed Mg and Cu alloys were investigated. Also, this study demonstrated that the work function is a promising indicative parameter, providing supplementary clues for understanding the effects of strain rate and sample thickness on the generation of dislocations and micro-voids or vacancy clusters during deformation under different conditions and their influences on material properties. Some of the key highlights of the thesis are-:

(1) Higher strain rate alloys have more micro-cracks/voids which deteriorate their hardness and wear resistance.

(2) Although micro-cracks less deteriorated the corrosion resistance, they considerably weakened the material against wear.

(3) The corrosion wear shows a lower wear loss than dry wear due to the lubrication effect of the solution.

(4) The SEM and EDS characterization on wear shows that the microcracks where prominent in corrosive wear in faster strained sample due to synergetic effect of wear and corrosion.

(5) Although XRD and SEM characterization are good for defects analysis, residual strain or dislocation density phenomenon were not clearly shown.

(6) EWF is promising indicative parameter for material characterization and for understanding the effects of strain rate on the generation of dislocations and micro-voids during deformation under different conditions and their influences on material properties.

5.2 Future Work

1. Study the possibility of the effect of strain rate on the tribological properties of alloys with FCC and BCC structures and compare them with the HCP structures.
2. More understanding in terms of mathematical expressions is needed to further understand the void and dislocations relationships with respect to strain rates.
3. Understanding and establishing relationship between EWF and strain rate for various material could be done.
4. Studying the strain rate effect on tribological properties of nano-particle incorporated Mg alloys.

Bibliography

[1] W. D. Callister, *Materials science and engineering: an introduction*. John Wiley and Sons, New York, 3rd edition 1997.

[2] C. P. Salisbury, M. J. Worswick, and R. Mayer, "High rate constitutive modeling of aluminium alloy tube," *J. Phys. Iv*, vol. 134, pp. 43–48, 2006.

[3] J.-H. Kim, D. Kim, H. N. Han, F. Barlat, and M.-G. Lee, "Strain rate dependent tensile behavior of advanced high strength steels: Experiment and constitutive modeling," *Mater. Sci. Eng. A*, vol. 559, pp. 222–231, 2013.

[4] R. Smerd, S. Winkler, C. Salisbury, M. Worswick, D. Lloyd, and M. Finn, "High strain rate tensile testing of automotive aluminum alloy sheet," *Int. J. Impact Eng.*, vol. 32, no. 1–4, pp. 541–560, 2005.

[5] M. K. Kulekci, "Magnesium and its alloys applications in automotive industry," *Int. J. Adv. Manuf. Technol.*, vol. 39, no. 9–10, pp. 851–865, 2008.

[6] E. Aghion and B. Bronfin, "Magnesium Alloys Development towards the 21st Century," *Mater. Sci. Forum*, vol. 350–351, pp. 19–30, 2000.

[7] M. P. Staiger, A. M. Pietak, J. Huadmai, and G. Dias, "Magnesium and its alloys as orthopedic biomaterials: A review," *Biomaterials*, vol. 27, no. 9. pp. 1728–1734, 2006.

[8] F. Witte *et al.*, “In vivo corrosion of four magnesium alloys and the associated bone response,” *Biomaterials*, vol. 26, no. 17, pp. 3557–3563, 2005.

[9] N. Hort, Y. Huong, and K. U. Kainer, “Intermetallics in magnesium alloys,” *Advanced Engineering Materials*, vol. 8, no. 4. pp. 235–240, 2006.

[10] X. M. Wang, X. Q. Zeng, Y. Zhou, G. S. Wu, S. S. Yao, and Y. J. Lai, “Early oxidation behaviors of Mg-Y alloys at high temperatures,” *J. Alloys Compd.*, vol. 460, no. 1–2, pp. 368–374, 2008.

[11] K. U. Kainer, “Challenges for implementation of magnesium into more applications,” in *Magnesium Technology 2016*, 2016, pp. 5–6.

[12] H. E. Friedrich and B. L. Mordike, *Magnesium technology: Metallurgy, design data, applications*. 2006.

[13] F. Zivić, N. Grujović, G. Manivasagam, C. Richard, J. Landoulsi, and V. Petrović, “The potential of magnesium alloys as bioabsorbable / biodegradable implants for biomedical applications,” *Tribol. Ind.*, vol. 36, no. 1, pp. 67–73, 2014.

[14] C. Bettles and M. Barnett, *Advances in wrought magnesium alloys: Fundamentals of processing, properties and applications*. 2012.

[15] T. Z. Blazynski, *Materials at high strain rates*. Springer Science & Business Media, 1987.

[16] G. Hua and D. Li, “Generic relation between the electron work function and Young’s modulus of metals,” *Appl. Phys. Lett.*, vol. 99, no. 4, 2011.

[17] N. D. Lang and W. Kohn, “Theory of metal surfaces: Work function,” *Phys. Rev. B*, vol. 3, no. 4, pp. 1215–1223, 1971.

[18] A. Subramanyam, *Kelvin Probe For Surface Engineering : Fund And Design*. Ane Books Pvt Ltd, 2010.

[19] P. S. Bagus, D. Käfer, G. Witte, and C. Wöll, “Work function changes induced by charged adsorbates: Origin of the polarity asymmetry,” *Phys. Rev. Lett.*, vol. 100, no. 12, 2008.

[20] P. E. C. Franken and V. Ponec, “Photoelectric work function measurements on nickel-copper and nickel-gold alloy films. Clean surfaces and adsorption of ethylene and carbon monoxide,” *J. Catal.*, vol. 42, no. 3, pp. 398–407, 1976.

[21] T. N. Rhodin and J. E. Demuth, “Chemisorption on (001), (110) and (111) nickel surfaces,” *Jpn. J. Appl. Phys.*, vol. 13, pp. 167–176, 1974.

[22] J. Janata, “Chemical Modulation of the Electron Work Function,” *Anal. Chem.*, vol. 63, no. 22, pp. 2546–2550, 1991.

[23] K. Y. Yu, C. R. Helms, W. E. Spicer, and P. W. Chye, “Photoemission studies of the surface and bulk electronic structure of the Cu-Ni alloys,” *Phys. Rev. B*, vol. 15, no. 4, pp. 1629–1639, 1977.

[24] C. Benndorf, G. Klatte, and F. Thieme, “Interaction of oxygen with CuNi(110) alloy surfaces: AES, XPS and work function measurements,” *Surf. Sci.*, vol. 135, no. 1–3, pp. 1–17, 1983.

[25] D. Y. Li, “Electron work function at grain boundary and the corrosion behavior of nanocrystalline metallic materials,” *MRS Online Proc. Libr. Arch.*, vol. 887, 2005.

[26] W. Li and D. Y. Li, “Influence of surface morphology on corrosion and electronic behavior,” *Acta Mater.*, vol. 54, no. 2, pp. 445–452, 2006.

[27] G. V Samsonov, V. S. Fomenko, I. A. Podchernyaeva, and L. N. Okhremchuk, “Thermionic emission properties of refractory compounds and materials based on them (a review),” *Sov. Powder Metall. Met. Ceram.*, vol. 13, no. 10, pp. 836–842, 1974.

[28] A. Kiejna and K. F. Wojciechowski, “Work function of metals: Relation between theory and experiment,” *Prog. Surf. Sci.*, vol. 11, no. 4, pp. 293–338, 1981.

[29] H. Watarai, “Trend of Research and Development for Magnesium Alloys - Reducing the Weight of Structural Materials in Motor Vehicles -,” *Sci. Technol. trends*, vol. Quarterly, no. 18, pp. 84–97, 2004.

[30] W. J. Joost and P. E. Krajewski, “Towards magnesium alloys for high-volume automotive applications,” *Scr. Mater.*, vol. 128, pp. 107–112, 2017.

[31] M. Pekguleryuz, K. Kainer, and A. A. Kaya, *Fundamentals of magnesium alloy*

metallurgy. 2013.

[32] R. Abbaschian and R. E. Reed-Hill, *Physical metallurgy principles*. Cengage Learning, 2008.

[33] R. W. K. Honeycombe, "The plastic deformation of metals," 1975.

[34] W. F. Hosford and R. M. Caddell, *Metal forming: mechanics and metallurgy*. Cambridge University Press, 2011.

[35] P. G. Partridge, "The crystallography and deformation modes of hexagonal close-packed metals," *Metall. Rev.*, vol. 12, no. 1, pp. 169–194, 1967.

[36] J. Koike *et al.*, "The activity of non-basal slip systems and dynamic recovery at room temperature in fine-grained AZ31B magnesium alloys," *Acta Mater.*, vol. 51, no. 7, pp. 2055–2065, 2003.

[37] M. H. Yoo, "Slip, twinning, and fracture in hexagonal close-packed metals," *Metall. Trans. A*, vol. 12, no. 3, pp. 409–418, 1981.

[38] X. Y. Lou, M. Li, R. K. Boger, S. R. Agnew, and R. H. Wagoner, "Hardening evolution of AZ31B Mg sheet," *Int. J. Plast.*, vol. 23, no. 1, pp. 44–86, 2007.

[39] B. Beausir, L. S. Tóth, F. Qods, and K. W. Neale, "Texture and Mechanical Behavior of Magnesium During Free-End Torsion," *J. Eng. Mater. Technol.*, vol. 131, no. 1, p. 11108, 2009.

[40] M. R. Barnett, “Twinning and the ductility of magnesium alloys. Part I: ‘Tension’ twins,” *Mater. Sci. Eng. A*, vol. 464, no. 1–2, pp. 1–7, 2007.

[41] S. Godet, L. Jiang, A. A. Luo, and J. J. Jonas, “Use of Schmid factors to select extension twin variants in extruded magnesium alloy tubes,” *Scr. Mater.*, vol. 55, no. 11, pp. 1055–1058, 2006.

[42] B. A. Bilby and A. G. Crocker, “The Theory of the Crystallography of Deformation Twinning,” *Proc. R. Soc. A Math. Phys. Eng. Sci.*, vol. 288, no. 1413, pp. 240–255, 1965.

[43] W. F. Hosford, *The mechanics of crystals and textured polycrystals*. 1993.

[44] D. R. Thornburg and H. R. Piehler, “An analysis of constrained deformation by slip and twinning in hexagonal close packed metals and alloys,” *Metall. Trans. A*, vol. 6, no. 8, pp. 1511–1523, 1975.

[45] W. Püschl, “Models for dislocation cross-slip in close-packed crystal structures: A critical review,” *Progress in Materials Science*, vol. 47, no. 4. pp. 415–461, 2002.

[46] R. Gehrmann, M. M. Frommert, and G. Gottstein, “Texture effects on plastic deformation of magnesium,” *Mater. Sci. Eng. A*, vol. 395, no. 1–2, pp. 338–349, 2005.

[47] C.-W. Tan *et al.*, “Deformation behavior of AZ31 magnesium alloy at different strain rates and temperatures,” *Trans. Nonferrous Met. Soc. China*, vol. 17, no. s1A, pp.

s347–s352, 2007.

[48] Z. He, J. Ma, H. Wang, G. E. B. Tan, D. Shu, and J. Zheng, “Dynamic fracture behavior of layered alumina ceramics characterized by a split Hopkinson bar,” *Mater. Lett.*, vol. 59, no. 8–9, pp. 901–904, 2005.

[49] S. Dong, Y. Wang, and Y. Xia, “A finite element analysis for using Brazilian disk in split Hopkinson pressure bar to investigate dynamic fracture behavior of brittle polymer materials,” *Polym. Test.*, vol. 25, no. 7, pp. 943–952, 2006.

[50] Q. M. Li and H. Meng, “About the dynamic strength enhancement of concrete-like materials in a split Hopkinson pressure bar test,” *Int. J. Solids Struct.*, vol. 40, no. 2, pp. 343–360, 2003.

[51] C. Van Sligtenhorst, D. S. Cronin, and G. W. Brodland, “High strain rate compressive properties of bovine muscle tissue determined using a split Hopkinson bar apparatus,” *J. Biomech.*, vol. 39, no. 10, pp. 1852–1858, 2006.

[52] K. Ishikawa, H. Watanabe, and T. Mukai, “High temperature compressive properties over a wide range of strain rates in an AZ31 magnesium alloy,” *J. Mater. Sci.*, vol. 40, no. 7, pp. 1577–1582, 2005.

[53] K. Ishikawa, H. Watanabe, and T. Mukai, “High strain rate deformation behavior of an AZ91 magnesium alloy at elevated temperatures,” *Mater. Lett.*, vol. 59, no. 12, pp. 1511–1515, 2005.

[54] M. a. Meyers, “Dynamic Behavior of Materials,” *Dyn. Behav. Mater.*, p. 55, 1994.

[55] F. C. Frank, “On the equations of motion of crystal dislocations,” *Proc. Phys. Soc. Sect. A*, vol. 62, no. 2, pp. 131–134, 1949.

[56] K. Isik, G. Gerstein, T. Clausmeyer, F. Nürnberger, A. E. Tekkaya, and H. J. Maier, “Evaluation of Void Nucleation and Development during Plastic Deformation of Dual-Phase Steel DP600,” *Steel Res. Int.*, vol. 87, no. 12, pp. 1583–1591, 2016.

[57] M. D. Taylor, D. K. Matlock, E. De Moor, and J. G. Speer, “Development of a Plane Strain Tensile Geometry to Assess Shear Fracture in Dual Phase Steels,” *J. Mater. Eng. Perform.*, vol. 23, no. 10, pp. 3685–3694, 2014.

[58] S. Kojima, “Formation of Voids in Thin Foil Pure Gold during Plastic Deformation,” *Mater. Trans.*, vol. 157, no. 1/2, pp. 25–301, 2006.

[59] W. T. Becker *et al.*, “ASM handbook,” *Fail. Anal. Prev.*, vol. 11, p. 1072, 2002.

[60] X. Sun, M. Nouri, Y. Wang, and D. Y. Li, “Corrosive wear resistance of Mg-Al-Zn alloys with alloyed yttrium,” *Wear*, vol. 302, no. 1–2, pp. 1624–1632, 2013.

[61] W. F. Gale and T. C. Totemeir, “Smithells Metals Reference Book,” *Smithells Met. Ref. B.*, pp. 1–2072, 2004.

[62] W. Li and D. Y. Li, “Effect of surface geometrical configurations induced by microcracks on the electron work function,” *Acta Mater.*, vol. 53, no. 14, pp. 3871–

3878, 2005.

[63] G. Hua and D. Li, “The correlation between the electron work function and yield strength of metals,” *Phys. status solidi*, vol. 249, no. 8, pp. 1517–1520, Aug. 2012.

[64] W. Li, Y. Wang, and D. Y. Li, “Response of the electron work function to deformation and yielding behavior of copper under different stress states,” *Phys. Status Solidi Appl. Res.*, vol. 201, no. 9, pp. 2005–2012, 2004.

[65] H. Lu and D. Li, “Correlation between the electron work function of metals and their bulk moduli, thermal expansion and heat capacity via the Lennard-Jones potential,” *Phys. Status Solidi Basic Res.*, vol. 251, no. 4, pp. 815–820, 2014.

[66] D. Y. Li and W. Li, “Electron work function: A parameter sensitive to the adhesion behavior of crystallographic surfaces,” *Appl. Phys. Lett.*, vol. 79, no. 26, pp. 4337–4338, Dec. 2001.

[67] W. Li and D. Y. Li, “Variations of work function and corrosion behaviors of deformed copper surfaces,” *Appl. Surf. Sci.*, vol. 240, no. 1–4, pp. 388–395, 2005.

[68] M. Brajczewska, C. Henriques, and C. Fiolhais, “Dependence of metal surface properties on the valence-electron density in the stabilized jellium model,” in *Vacuum*, 2001, vol. 63, no. 1–2, pp. 135–138.

[69] S. Halas and T. Durakiewicz, “Work functions of elements expressed in terms of the Fermi energy and the density of free electrons,” *J. Phys. Condens. Matter*, vol. 10,

no. 48, pp. 10815–10826, 1998.

[70] W. Li and D. Y. Li, “Effects of elastic and plastic deformations on the electron work function of metals during bending tests,” *Philos. Mag.*, vol. 84, no. 35, pp. 3717–3727, 2004.

[71] H. Lu, G. Hua, and D. Li, “Dependence of the mechanical behavior of alloys on their electron work function—An alternative parameter for materials design,” *Appl. Phys. Lett.*, vol. 103, no. 26, p. 261902, Dec. 2013.

[72] A. R. Miedema, “The electronegativity parameter for transition metals: Heat of formation and charge transfer in alloys,” *J. Less-Common Met.*, vol. 32, no. 1, pp. 117–136, 1973.

[73] W. Li and D. Y. Li, “Exploring the application of the Kelvin method in studying the history prior to wear and the onset of wear,” *Wear*, vol. 253, no. 7–8, pp. 746–751, 2002.

[74] X. Y. Wang and D. Y. Li, “Mechanical, electrochemical and tribological properties of nano-crystalline surface of 304 stainless steel,” *Wear*, vol. 255, no. 7–12, pp. 836–845, 2003.

[75] P. Schmutz and G. S. Frankel, “Corrosion Study of AA2024-T3 by Scanning Kelvin Probe Force Microscopy and In Situ Atomic Force Microscopy Scratching,” *J. Electrochem. Soc.*, vol. 145, no. 7, pp. 2295–2306, 1998.

[76] Q. N. Song, Y. G. Zheng, D. R. Ni, and Z. Y. Ma, “Studies of the nobility of phases using scanning Kelvin probe microscopy and its relationship to corrosion behaviour of Ni-Al bronze in chloride media,” *Corros. Sci.*, vol. 92, pp. 95–103, 2015.

[77] J. Umeda, N. Nakanishi, K. Kondoh, and H. Imai, “Surface potential analysis on initial galvanic corrosion of Ti/Mg-Al dissimilar material,” *Mater. Chem. Phys.*, vol. 179, pp. 5–9, 2016.

[78] L. Q. Guo, M. Li, X. L. Shi, Y. Yan, X. Y. Li, and L. J. Qiao, “Effect of annealing temperature on the corrosion behavior of duplex stainless steel studied by in situ techniques,” *Corros. Sci.*, vol. 53, no. 11, pp. 3733–3741, 2011.

[79] M. Rohwerder and F. Turcu, “High-resolution Kelvin probe microscopy in corrosion science: Scanning Kelvin probe force microscopy (SKPFM) versus classical scanning Kelvin probe (SKP),” *Electrochim. Acta*, vol. 53, no. 2, pp. 290–299, 2007.

[80] G. Kresse and D. Joubert, “From ultrasoft pseudopotentials to the projector augmented - wave method,” *Phys. Rev. B*, vol. 59, p. 1758, 1999.

[81] D. Alfè, M. J. Gillan, and G. D. Price, “Constraints on the composition of the Earth’s core from ab initio calculations,” *Nature*, vol. 405, no. 6783, pp. 172–175, 2000.

[82] L. Vočadlo, D. Alfè, M. J. Gillan, I. G. Wood, J. P. Brodholt, and G. D. Price, “Possible thermal and chemical stabilization of body-centred-cubic iron in the Earth’s core,” *Nature*, vol. 424, no. 6948, pp. 536–539, 2003.

[83] J. Hafner, “Ab-initio simulations of materials using VASP: Density-functional theory and beyond,” *Journal of Computational Chemistry*, vol. 29, no. 13. pp. 2044–2078, 2008.

[84] G. Kresse and J. Furthmüller, “Efficient iterative schemes for ab initio total-energy calculations using a plane-wave basis set,” *Phys. Rev. B - Condens. Matter Mater. Phys.*, vol. 54, no. 16, pp. 11169–11186, 1996.

[85] J. Perdew, K. Burke, and M. Ernzerhof, “Generalized Gradient Approximation Made Simple.,” *Phys. Rev. Lett.*, vol. 77, no. 18, pp. 3865–3868, 1996.

[86] W. Woo, L. Balogh, T. Ungár, H. Choo, and Z. Feng, “Grain structure and dislocation density measurements in a friction-stir welded aluminum alloy using X-ray peak profile analysis,” *Mater. Sci. Eng. A*, vol. 498, no. 1–2, pp. 308–313, 2008.

[87] H. Lu, Z. Liu, X. Yan, D. Li, L. Parent, and H. Tian, “Electron work function-a promising guiding parameter for material design,” *Sci. Rep.*, vol. 6, 2016.

[88] E. Rabinowicz and R. I. Tanner, “Friction and wear of materials,” *J. Appl. Mech.*, vol. 33, p. 479, 1966.

[89] D. H. Buckley, “Surface effects in adhesion, friction, wear and lubrication,” *Tribol. Ser.*, vol. 5, p. 267, 1981.

[90] I. D. Baikie, P. J. S. Smith, D. M. Porterfield, and P. J. Estrup, “Multitip scanning bio-Kelvin probe,” *Rev. Sci. Instrum.*, vol. 70, no. 3, pp. 1842–1850, 1999.

[91] J. W. Christian, “The stress dependence of dislocation velocity, and its relation to the strain rate sensitivity,” *Acta Metall.*, vol. 12, no. 1, pp. 99–102, 1964.

[92] D. Hull and D. J. Bacon, *Introduction to Dislocations*. 2011.

Appendix A

Abbreviations

EWF	Electron Work Function
KP	Kelvin Probe
KPFM	Kelvin Probe Force Microscope
SEM	Scanning Electron Microscope
SKP	Scanning Kelvin Probe
XRD	X-ray Diffraction
HCP	Hexagonal close-packed
CRSS	Critical resolved shear stress
BCC	Body centered cubic
FCC	Face centered cubic
VASP	Vienna Ab initio Simulation Package
PAW	Projector-augmented wave
GGA	Generalized gradient approximation
EDS	Energy-dispersive X-ray spectroscopy

Appendix B

List of Symbols

v	velocity of the dislocation
v_0	velocity of sound
m_0	Equivalent mass of a screw dislocation at rest
$\rho_{dislocation}$	Dislocation density
V	The wear volume loss
H	Hardness of the material
L	Normal Load
S	Sliding distance
K	Wear coefficient
V_{ct}	Total loss in volume due to corrosive wear
V_{lw}	Loss in volume due to wear
V_{lc}	Loss in volume due to corrosion

r_{c-w}	The increase in wear rate due to corrosion
r_{w-c}	The increase in corrosion rate due to wear
$r_{synergy}$	Loss in volume resulted by synergy of wear and corrosion
l_0	Original length of the grid before deformation
l	Length after deformation
$\vec{f}$	Force required to drive the dislocation to move in the crystal lattice
$(\partial\vec{V}/\partial t)$	Acceleration for the dislocation to reach a certain speed